Nano-domain structure and deformation mechanism in Ti-Nb-Zr-Ta-O alloys

WEILESI

February 2016

Nano-domain structure and deformation mechanism in Ti-Nb-Zr-Ta-O alloys

WEILESI

Doctoral Program in Materials Science

Submitted to the Graduate School of

Pure and Applied Sciences

in Partial Fulfillment of the Requirements

for the Degree of Doctor of Philosophy in

Engineering

at the

University of Tsukuba

Table of content

Chapter 1

General introduction

1.1 General aspects of Ti-base alloys

With the development of technology and economy, the metallic materials have been extensively studied and applied in many fields. Ti and its alloys are considered to be important functional metallic materials due to their excellent properties such as high strength/weight ratio, low density and good corrosion resistance. The pure Ti undergoes an allotropic transformation at 1155K: from α phase to β phase upon heating where the α phase is the hcp structure and the β phase is a bcc structure [1].

The alloying elements can be dissolved in Ti and affect the transformation temperature. Al or interstitial atoms such as O, N and C can stabilize the α phase. These α stabilizers are quite strong solid solution strengtheners either in the α phase or in the β phase. Cr, Nb, Cu, Fe, Mn, Mo, Ta and V stabilize the β phase to ensure the retention of the bcc phase by the decrease in the transformation temperature from α phase to β phase. Sn and Zr have little effect in the α/β transformation temperature. Fig. 1-1 shows that a phase diagram of β-type Ti-X alloys (X= Mo, Nb, Ta, V, etc.) exhibiting the martensitic transformation. With increasing amount of β-stabilizers in pure Ti, the martensitic transformation temperature (*M*s) decreases as indicated by a dashed line and the β phase becomes more stable. The region of the β phase becomes broader at a low temperature region. Quenching from the β phase rapidly through the α+β region results in a martensitic transformation whereas slower cooling results in the nucleation and the growth of α phase. According to the amount of β-stabilizers, a crystalline structure of martensite phase becomes either orthorhombic or hcp

structure, designated by α″ and α′, respectively. The shape memory effect and superelasticity in Ti-based alloys are associated with the orthorhombic α″ martensite. Whereas α-stabilizers more or less elevate the temperature of the β/α+β transition.

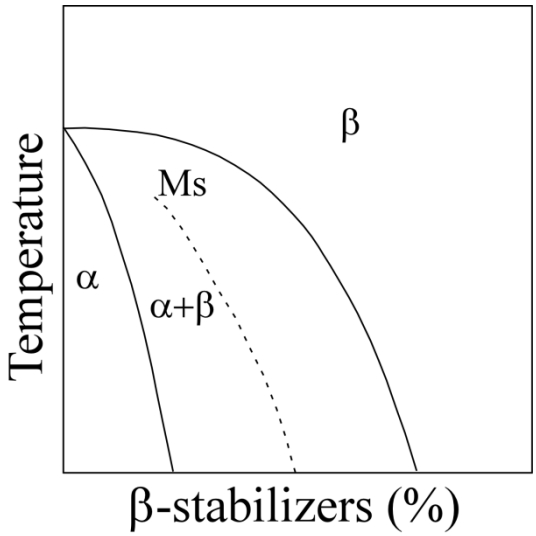

Fig. 1-1 A schematic phase diagram of Ti-X alloys (X= Mo, Nb, Ta, V, etc.).

1.2 Introduction to shape memory alloys

Supposing that a normal metallic material is bent or stretched by loading beyond its elastic range, the shape cannot recover to their original either by unloading or heating due to the introduction of dislocations and defects, leading to permanent plastic deformation. Whereas the shape memory alloys are a group of metallic alloys can recover to their pre-deformed shape by heating after unloading or only upon the removal of stress. The phenomenon of the shape recovery upon heating is known as shape memory effect whereas the

shape recovery without heating is known as surperelasticity. Both of these two characteristics are the result from martensitic transformation which is considered being a non-diffusion transformation process between solid phases and can be affected by the temperature, exerted stress and magnetic field. The shape memory alloys have been used extensively in automotive, aerospace, robotics, biomedical industries [2].

The superelasticity was discovered in Au-Cd alloy in 1932 by Olander [3], and the shape memory effect was first observed in Cu-Zn alloy in 1938 by Greninger and Mooradian [4]. The most famous and widely used shape memory alloy is Ti-Ni alloys due to their excellent shape memory effect and superelasticity [5, 6] and good biocompatibility [7] However, the potential problems over hypersensitivity and toxicity of Ni have been pointed out, although Ti-Ni shape memory alloys have been already applied generally as biomedical materials like bone plates, stents and orthodontic arch wires. In recent years, β-type Ti-based shape memory alloys without Ni or toxic element have been developed in biomedical filed [8-10]. The addition of alloying elements such as Zr [9], Ta [11], Pt [11], Sn [13-15], Mo [16-20] and Nb [21-23] and varies thermo-mechanical treatments have been reported to improve the properties of β-type Ti-based alloys, such as recovery stain, functional stability, and the critical stress for slip.

1.3 Martensitic transformation on β-type Ti-based alloys

1.3.1 Introduction of martensitic transformation

The martensitic transformation is the process of phase transformation between the parent phase and martensite which complies with a first order solid to solid phase transition. The interface between the parent phase and the martensite phase is constituted by an invariant plane (habit plane), and the martensitic

transformation proceeds by the movement of the habit plane. This process of the movement does not affect the alloy composition. The external stress can facilitate the martensitic transformation. The martensitic transformation accompanied by a hysteresis. In general, the martensitic transformation is described by the four temperatures: martensitic transformation start temperature (*M*s) and martensitic transformation finish temperature (*M*f) and similarly those of reverse transformation start temperature (*A*s) and reverse transformation finish temperature (*A*f). These kinds of temperatures are not only dependent on the alloy composition but also affected by internal stresses and lattice defects. The martensitic transformation results in no net macroscopic shape change due to the self-accommodation by multi-variants.

1.3.2 *The lattice corresponding in the martensitic transformation on β-type Ti-based alloys*

Fig. 1-2 shows a schematic explanation of a bcc β to an orthorhombic α″ transformation in Ti-based shape memory alloys. The orientation relationship between the β phase and α″ phase is as follows:

$$[100]_{\beta} // [100]_{\alpha''}, [011]_{\beta} // [010]_{\alpha''}, [0\bar{1}1]_{\beta} // [001]_{\alpha''}$$

When martensitic transformation occurs, the shuffling of the $\{110\}_{\beta}$ planes occur along the $\langle 1\bar{1}0\rangle_{\beta}$ orientation (arrow pointed) as shown in Fig. 1-2. Actually, α″ phase exhibits 6 kinds of shuffling mode variants. The relationships are summarized in Table 1-1. The lattice constant of the high symmetry bcc β phase is designated by “a” and those of low-symmetry orthorhombic α″ phase are designated by “ a’ ”, “ b’ ” and “ c’ ”, respectively. When martensitic transformation occurs a’ contracts compared with a, b’ expands and c’ is changeless.

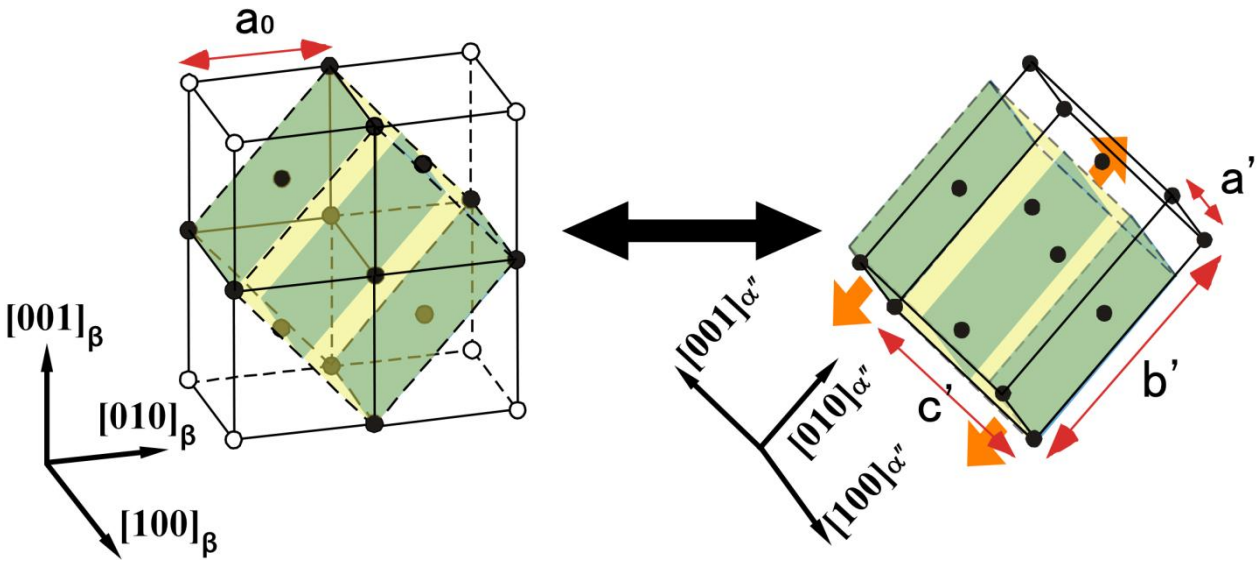

Fig.1-2. The lattice corresponding between parent phase and martensite phase.

Table 1-1. Six martensite variants V1-V6 and lattice correspondences with parent phase.

	$[100]_{\alpha''}$	$[010]_{\alpha''}$	$[001]_{\alpha''}$
V1	$[100]_{\beta}$	$[011]_{\beta}$	$[0\bar{1}1]_{\beta}$
V2	$[\bar{1}00]_{\beta}$	$[0\bar{1}1]_{\beta}$	$[011]_{\beta}$
V3	$[010]_{\beta}$	$[101]_{\beta}$	$[10\bar{1}]_{\beta}$
V4	$[0\bar{1}0]_{\beta}$	$[10\bar{1}]_{\beta}$	$[101]_{\beta}$
V5	$[001]_{\beta}$	$[110]_{\beta}$	$[\bar{1}10]_{\beta}$
V6	$[00\bar{1}]_{\beta}$	$[\bar{1}10]_{\beta}$	$[110]_{\beta}$

1.4 Shape memory effect and superelasticity of β-type Ti-based alloys

1.4.1 Mechanism of shape memory effect and superelasticity

Fig. 1-3 shows the schematic illustration of the shape memory effect and superelasticity which occur in a shape memory alloy. Fig.1-3(a) shows the single crystal parent phase which is stable at high temperature. When the parent phase (a) is cooled to the temperature below *M*f, the martensite variants (b) are formed on the manner of self-accommodating. The martensite phase in (b) is designated as thermally induced martensite. For simplicity only two variants which are designated as variant A and variant B are shown in (b). The variant A and variant B are twin related and the martensite is named as twinned martensite. The transformation strain is accommodated through self-accommodation in the martensite. The self-accommodation is realized through twinning created between the different variants [24, 25]. Accordingly, no shape changes in the material. If an external stress is applied in the thermally induced martensite or twinned martensite, the different variants of martensite reorient themselves to accommodate the most favorable variant [24] and to formed a single variant of martensite (variant A is shown in this case) in (d). This martensite which is shown in (d) is referred to as the deformed martensite or detwinned martensite. The transformation strain is induced in this process. The shape change is induced and the volume of the specimen in (d) is greater than (a) and (b). When the applied stress is removed, the deformed or detwined martensite is remained due to the stabilization in this temperature. When this deformed martensite(d) is heated to the temperature above *A*f, the reverse transformation takes place and the original shape of material is regained to (a). The process of (a) → (b) → (d) → (a) represents as shape memory effect.

Superelasticity is described by the process of (a) → (c) → (a). In this case the material is deformed above

*A*f. When the parent phase is subjected to a stress, the martensite phase which designated as stress induced martensite induced directly. This kind of martensite is only composed of one favorable variant (variant A in this case) as shown in Fig. 1-3(c). The transformation strain is induced in this process and shape change occurs. The shape recovery occurs by the removal of the external stress in the specimen due to the instability of this martensite(c) at temperature above *A*f. The martensite (c) reverts back to the parent phase.

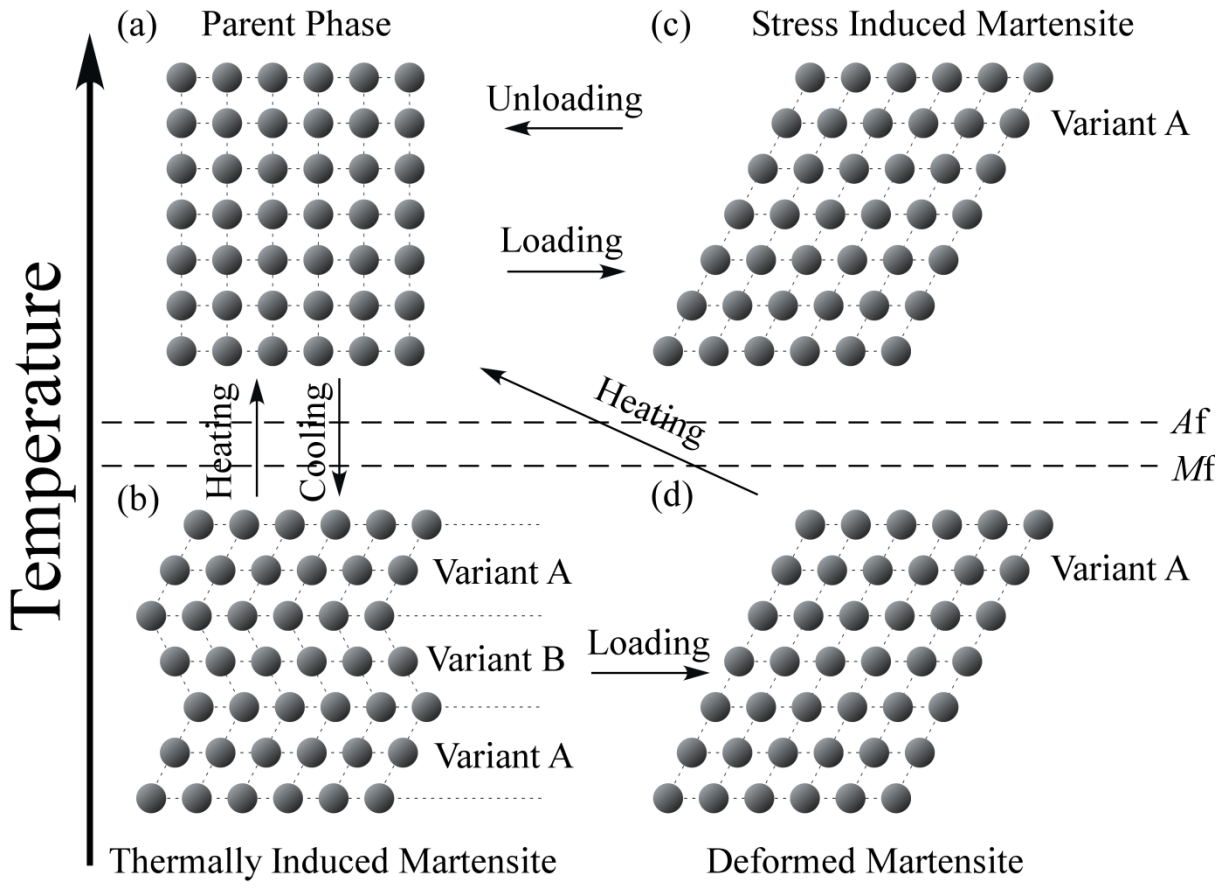

Fig. 1-3. Schematic illustration of shape memory effect and superelasticity occurred in a shape memory alloy.

1.4.2 Deformation behavior of the shape memory alloys

The deformation behavior of the shape memory alloys is deeply affected by test temperature. Fig. 1-4 (a) shows the relationship between test temperature and deformation behavior considering the martensitic transformation temperature of the shape memory alloys. Fig. 1-4 (b) shows the schematic illustration of the stress-strain curve at different temperatures. σ_{slip} is named the critical stress for slip deformation. σ_M is named the stress for inducing martensite. The σ_{slip} decreases with increasing temperature due to the easier mobility of defects such as dislocation at high temperature. The σ_M increases with increasing temperature, following the Clausius-Clapeyron relationship.

The tensile deformation behaviors of shape memory alloys in the test temperature region of T_1-T_5 are described by Fig. 1-4(a) and (b) as follow:

In the temperature region T_1, the material is composed of a single phase that is thermally induced martensite. When the material is deformed in this region the martensite thermally induced variants goes through a reorientation process and a single variant is formed. The shape of the material changes and the transformation strain is induced. When the material is heated to a temperature above the *A*f, the transformation strain which induced in this region T_1 recovers completely. This deformation behavior represents the shape memory effect. In the temperature region T_2, the material is also composed of a single martensite phase. The deformation behavior of the material in this region also represents the shape memory effect. When the material is deformed in this region the stress required for arranging the martensite variants reveals a smaller value than that at the region T_1 due to nearing the *M*s. The deformation behavior in this region also represents the shape memory effect. In the temperature region T_3, the material consists of the parent phase and martensite phase due to the test temperature is between *A*s and *A*f. The deformation

behavior in this region exhibits a mixture of shape memory effect and superelasticity because both the parent and the martensite phase are stable. In the temperature region T_4, the material is composed of the single parent phase. When the material is deformed the martensite phase is reduced. Then the reverse martensitic transformation occurs after the applied stress has been removed. The deformation behavior in this region exhibits perfect superelasticity. In the temperature region T_5, the σ_M increases and the σ_{slip} decreases. The plastic deformation occurs before the stress induced martensitic transformation. The deformation strain cannot be recovered by unloading or heating.

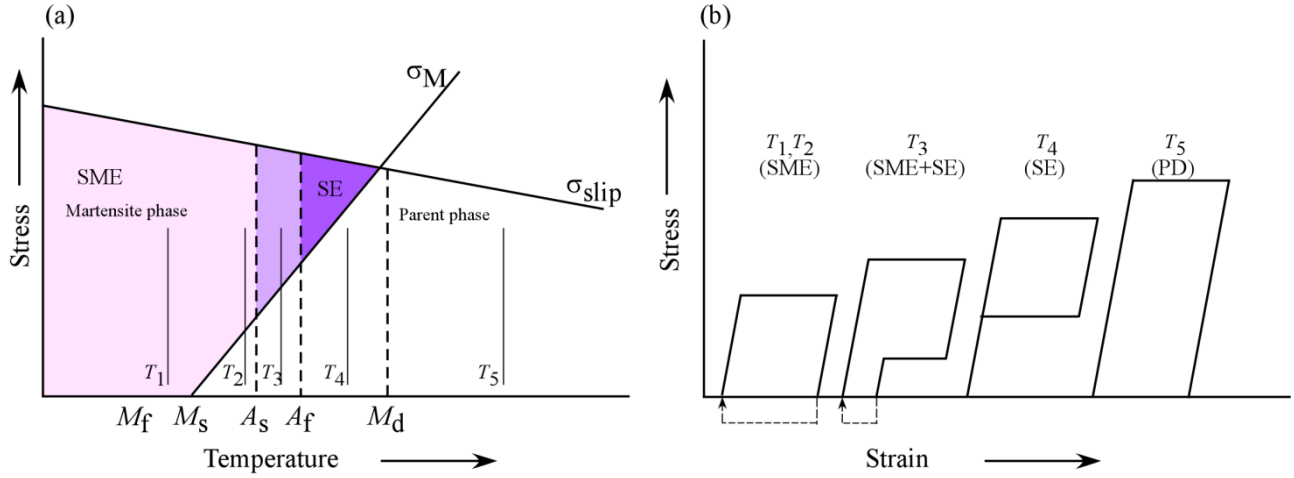

Fig. 1-4. (a) Relationship between test temperature and the shape memory and superelasticity behavior considering the martensitic transformation temperature. (b) Schematic illustration of the stress-strain curve at different temperatures.

1.5 Introduction of omega phase

ω phase can be formed by quenching in the metastable β-type Ti-based alloy which is referred to as the athermal ω phase or by aging which is called as the isothermal ω phase. The athermal ω phase is formed by a

diffusionless transformation which cannot be suppressed no matter how rapid the quench rate is. The composition of the athermal ω phase is same as that of the matrix [26]. On the other hand, the isothermal ω phase is formed by a diffusion-controlled process. The composition of the athermal ω phase is different from that of the matrix [27]. It is considered that the isothermal ω phase affects the mechanical properties more than the athermal ω phase. It is also noted that both ω phases suppress the martensitic transformation and decrease the *M*s [28]. The structure of the ω phase is either hexagonal or trigonal depending on the composition of the alloy [29, 30].

The orientation relationship between the bcc phase and the ω phase is as follows:

$$(0001)\omega \parallel (111)\beta\,;\ [2\bar{1}\bar{1}0]\omega \parallel [1\bar{1}0]\beta$$

It is noted that four variants of ω phase are present in the matrix according to the above orientation relationship.

1.6 The origin of nano-domain

1.6.1 Interstitial atoms in β-type Ti-based alloys

It is well known that interstitial elements such as oxygen [10, 31-40], nitrogen [41-44], carbon and hydrogen [45] can affect the mechanical properties of titanium alloys. For example, oxygen and nitrogen can increase the critical stress for plastic deformation [10, 41, 42, 44] and suppress the formation of α″ martensite and ω phases [32, 44, 46]. The addition of interstitial atoms in β-type Ti-based alloys significantly

improves the properties of alloys. In addition, the addition of interstitial alloying elements affects the deformation mechanism of meta-stable β-type Ti-based alloys. It has been reported that the deformation behavior changed from normal superelasticity to non-linear elasticity due to the addition of oxygen or nitrogen in Ti-Nb binary alloys [38-40, 43, 44]. This non-linear elastic deformation behavior is associated with nanodomain structure due to addition of interstitial atoms which can suppress the long range martensitic transformation.

1.6.2 Nano-domain

It has been reported that the interstitial atoms such as oxygen, nitrogen occupy the octahedral bcc matrix [47] due to the smaller size than other element atom. These interstitial oxygen atoms induce the local elastic strain fields. It has been also suggested that shuffling of $\{110\}\beta$ planes along $\langle 1\bar{1}0\rangle\beta$ directions occurs to relax the local strain fields caused by the interstitial atoms [34, 38, 39]. This shuffling mode is essentially identical to that of the martensitic transformation. Similar to the martensite variants, there are six orientation variants for nanodomains. The lattice correspondences between the shuffling modes of nano-domain and the variants in the martensitic transformation are listed in Table 1-2 [34]. There are three different octahedral sites (A, B and C) in a bcc structure as shown in Fig. 1-5. Different strain fields are formed around oxygen atoms according to the type of octahedral sites. For example, an oxygen atom which occupies the site A generates a local strain field along [001] direction. This local strain field can be relaxed by the shuffling modes V1, V2, V3 and V4 as shown in Fig. 1-6. For the B and C sites, the local strain filed is induced along [100] and [010], respectively. Similarly four orientation variants of nano-domain are capable of relaxing the local stress fields along [100] or [010]. As a result all of six nano-domain variants form uniformly and

equivalently if no external stress applied [39]. It is supposed that the suppression of the long range martensitic transformation is due to the fact that the growth of a particular variant of nano-domain is suppressed by adjacent other orientation variants of nano-domain.

Table 1-2. The lattice correspondence between the martensite variant and parent phase, and the corresponding shuffling modes.

Corresponding variant	Lattice corresponding			Shuffling modes
	$[100]_{\alpha''}$	$[010]_{\alpha''}$	$[001]_{\alpha''}$	
V1	$[100]_{\beta}$	$[011]_{\beta}$	$[0\bar{1}1]_{\beta}$	$(0\bar{1}0)[011]_{\beta}$
V2	$[\bar{1}00]_{\beta}$	$[0\bar{1}1]_{\beta}$	$[011]_{\beta}$	$(011)[0\bar{1}1]_{\beta}$
V3	$[010]_{\beta}$	$[101]_{\beta}$	$[10\bar{1}]_{\beta}$	$(10\bar{1})[101]_{\beta}$
V4	$[0\bar{1}0]_{\beta}$	$[10\bar{1}]_{\beta}$	$[101]_{\beta}$	$(101)[10\bar{1}]_{\beta}$
V5	$[001]_{\beta}$	$[110]_{\beta}$	$[\bar{1}10]_{\beta}$	$(\bar{1}10)[110]_{\beta}$
V6	$[00\bar{1}]_{\beta}$	$[\bar{1}10]_{\beta}$	$[110]_{\beta}$	$(110)[\bar{1}10]_{\beta}$

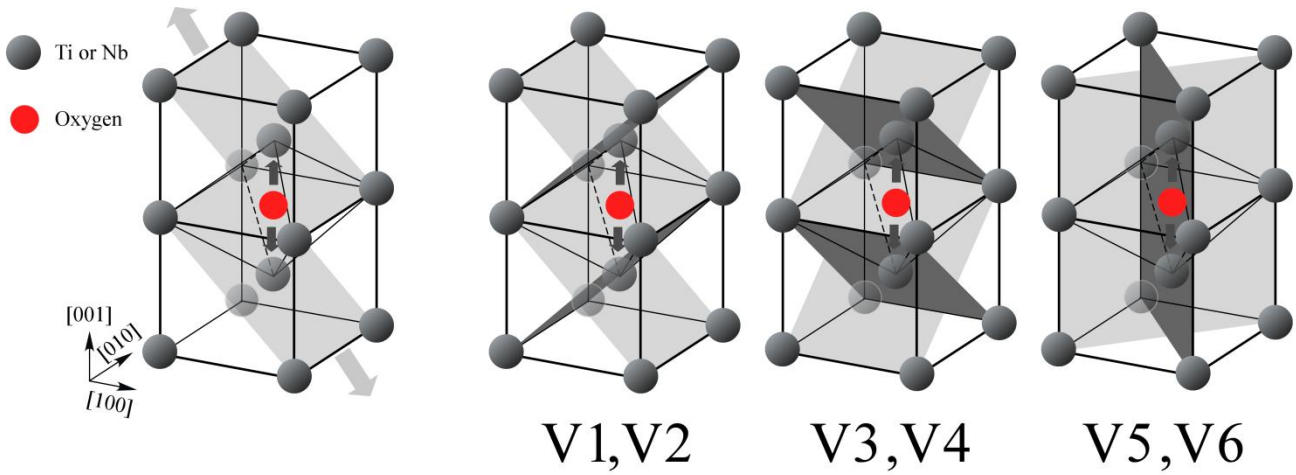

Fig. 1-6. Schematic illustration of shuffling modes (V1-V6) when the interstitial oxygen atom occupies the octahedral bcc matrix in site A.

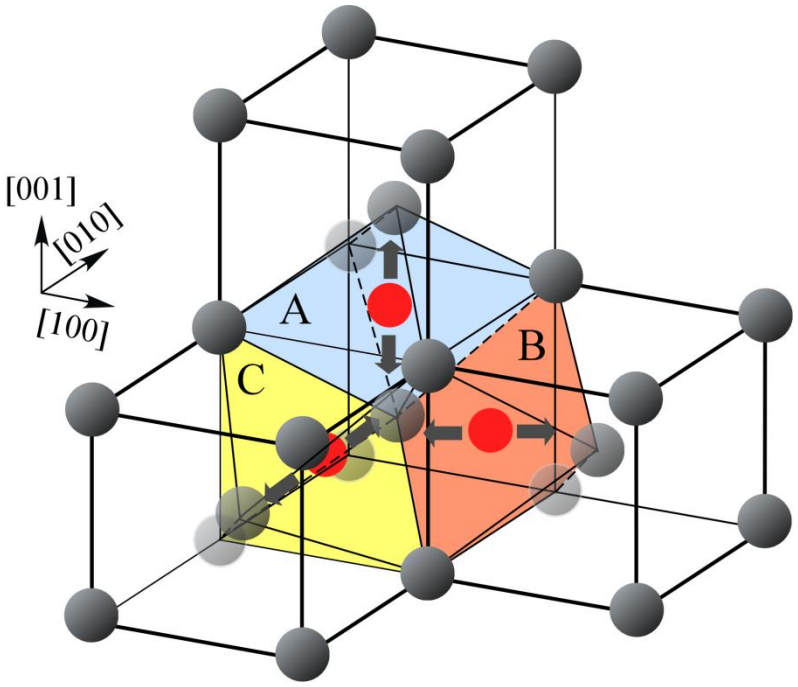

Fig. 1-5. Schematic illustration of shuffling modes when the interstitial oxygen atom occupies the octahedral bcc matrix in site A, B or C

1.7 General aspects of Gum metal

Gum metals consist of the Group IVa and Va elements and some amount of oxygen atoms. The chemical composition of Gum metals is characterized by (1) e/a ≈4.24; (2) a bond order (Bo) based on the DV-Xa cluster method is about 2.87; (3) the energy level of *d* electron orbital (Md) is about 2.45 eV. The typical composition of Ti-23Nb-2Zr-0.7Ta-1.2O has been developed by Toyota Central R&D laboratory and much attention has been paid to its unusual mechanical and physical properties such as non-linear elasticity, high strength, low elastic modulus, super-plasticity, Invar-like behavior and Elinvar properties shown in Fig. 1-7 [47]. These unique characteristics have made Gum metals attractive candidates for a wide range of applications such as eyeglass frames, medical equipment, artificial bones, and sporting goods.

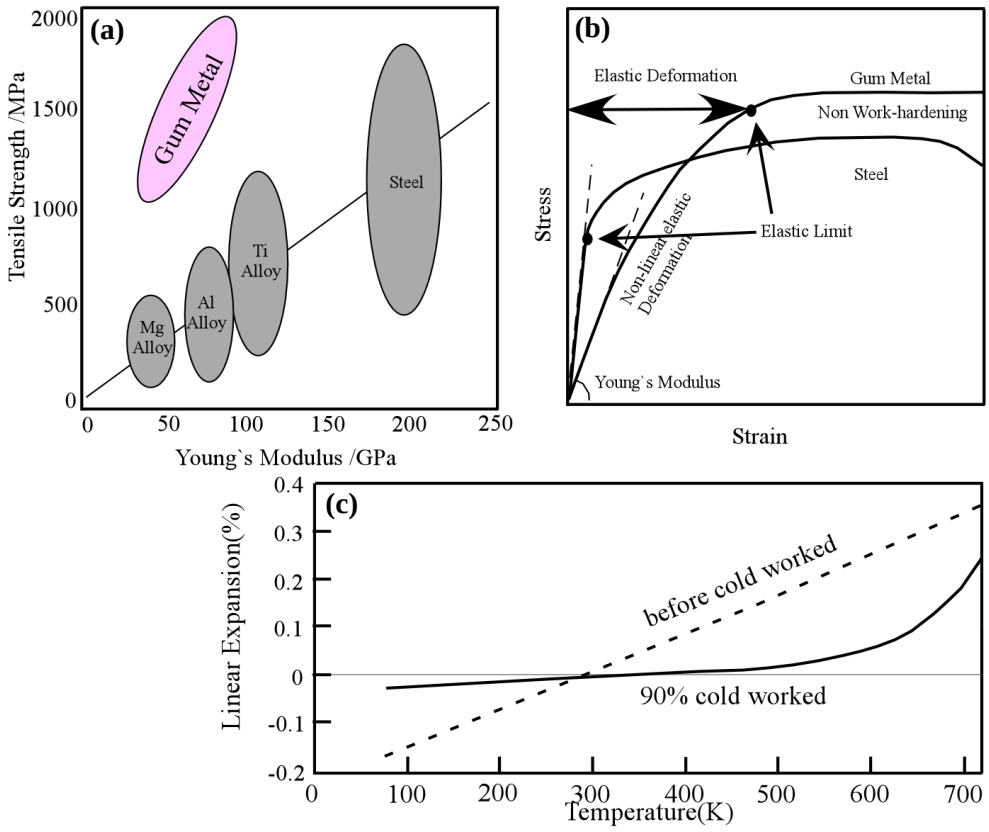

Fig. 1-7. Schematic illustration of the unique properties of Gum metal such as high strength and low Young's modulus (a), non-lineal elasticity comparing with steel in (b), Invar-like behavior after cold working at broad temperature range in (c)[47].

1.8 Research background and objectives

There have been extensive researches on the deformation behavior of Gum metal; however the mechanisms of unique properties of Gum metal are a subject of debate. It has been claimed by Furuta et al. [48] and Kuramoto et al. [49] that the superelastic behavior of Gum metal is not associated with the martensitic transformation. On the other hand, Talling et al. [35, 50] claimed that the deformation mechanisms of Gum metal are related to martensitic transformation on the basis of in situ synchrotron X-ray diffraction and TEM studies. They demonstrated that Gum metal deforms via reversible stress induced

martensitic transformation and the oxygen has significantly inhibited the amount of the transformation strain. Tane et al. [32, 46] investigated the effects of oxygen concentration and cold working on Young's modulus of Gum metal. They showed that high oxygen concentration can suppress the martensitic transformation and ω phase, resulting in low Young's modulus. Nii et al. [38] and Tahara et al. [39] have investigated the microstructure and deformation mechanism of the binary Ti-Nb alloys which also show the similar unique properties with Gum metal. They showed that the nanosized domain structure is produced by the addition oxygen and the nano-domain distributes randomly in the β phase. It has been recognized that the addition of oxygen plays a crucial role in achieving their unique properties however the underlying mechanism of unique properties of Gum metals is still a subject of debate. We have proposed that the unique properties of Gum metals can be successfully explained by considering the nano-domain structure. Recently, Kim et al. [34] reported the presence of martensite-like nano-domains in Gum metals through systematic transmission electron microscopy experiments. They demonstrated that the nano-domain structure is introduced to release the local stress field induced by interstitial oxygen atoms and the suppression of long-range martensitic transformation in Gum metals is due to the presence of the multi-variant nano-domain structure. They also revealed that the invar-like behavior of Gum metals can be explained by the nano-domain structure. However, the effects of oxygen concentration and β stability of Gum metals on the nano-domain structure and thermal expansion behavior have not yet been investigated. Furthermore, the effect of temperature on the deformation behavior of Gum metals has not been fully elucidated.

In this study, the effects of Nb and O contents on nanodomain structure, thermal expansion behavior and mechanical properties were investigated and the mechanism of anomalous thermal expansion behavior was discussed. In addition, the effects of O content and test temperature on the deformation behavior were also investigated and discussed.

References

[1] E.W. Collings, American Society for Metals, (1984).

[2] J.M. Jani, M. Leary, A. Subic, M. A. Gibson, Materials and Design, 56 (2014) 1078–1113.

[3] A. Olander, Z Kristallogr, 83(1932) 145.

[4] A.B. Greninger, V.G. Mooradian, Trans AIME, 128(1938)337.

[5] S. Miyazaki In: T.W. Duerig et al., editors. Ehgineering aspects of shape memory alloys. London: butterworth-Heinemann; 1990. P. 394.

[6] S. Miyazaki, Y. Ohmi, K. Otsuka, Y. Suzuki, J Phys 43(Suppl. 12)(1982) C4-255.

[7] T. Duerig, A. Pelton, D. Stockel, Mater. Sci. Eng. A, 149(1999)273-275.

[8] H.Y. Kim, Y. Ikehra, J.I. Kim, H. Hosoda, S. Miyazaki, Acta. Mater., 54 (2006), p. 2419

[9] J.I. Kim, H.Y. Kim, T. Inamura, H. Hosoda, S. Miyazaki, Mater Sci Eng A, 403 (2005), p. 334

[10] J.I. Kim, H.Y. Kim, H. Hosoda, S. Miyazaki, Mater Trans, 46 (2005), p. 852

[11] H.Y. Kim, S. Hashimoto, J.I. Kim, T. Inamura, H. Hosoda, S. Miyazaki, Mater Sci Eng A, 417 (2006), p. 120

[12] H.Y. Kim, N. Oshika, J.I. Kim, T. Inamura, H. Hosoda, S. Miyazaki, Materials transactions, vol. 48Japan Institute of Metals, Sendai, JAPON (2007) p. 400

[13] E. Takahashi, T. Sakurai, S. Watanabe, N. Masahashi, S. Hanada, Mater Trans, 43 (2002), p. 2978

[14] Y. Al-Zain, Y. Sato, H.Y. Kim, H. Hosoda, T.H. Nam, S. Miyazaki, Acta Mater, 60 (2012), p. 2437

[15] T. Maeshima, S. Ushimaru, K. Yamauchi, M. Nishida, Mater Trans, 47 (2006), p. 513

[16] H.Y. Kim, Y. Ohmatsu, J.I. Kim, H. Hosoda, S. Miyazaki, Mater Trans, 45 (2004), p. 1090

[17] Y. Sutou, K. Yamauchi, T. Takagi, T. Maeshima, M. Nishida, Mater Sci Eng A, 438-40 (2006), p. 1097

[18] T. Maeshima, S. Ushimaru, K. Yamauchi, M. Nishida, Mater Sci Eng A, 438-40 (2006), p. 844

[19] T. Maeshima, M. Nishida, Mater Trans, 45 (2004), p. 1096

[20] T. Maeshima, m. Nishida, Mater Trans, 45 (2004), p. 1101

[21] H.Y. Kim, Y. Ohmatsu, J.I. Kim, T. Inamura, H. Hosoda, S. Miyazaki, Mater Trans, 47 (2006), p. 518

[22] H. Tobe, H.Y. Kim, T. Inamura, H. Hosoda, T.H. Nam, S. Miyazaki, J. Alloys Compd. 577s (2013), p. s435

[23] H.Y. Kim, H. Satoru, J.I. Kim, H. Hosoda, S. Miyazaki, Mater Trans, 45 (2004), p. 2443

[24] S. Miyazaki, K. Otsuka, C.M. Wayman, Acta Metall, 37(1989), p.1873

[25] S. Miyazaki, K. Otsuka, ISIJ International, 29(1989), p.353

[26] T.W. Duerig, D.T. Terlinde, J.C. Williams, Titanium '80 Science & Technology - Proceedings of the 4th Int'l Conference on Titanium(eds.), 2(1980) 1299-1308.

[27] D. De Fontaine, N.E. Paton, J.C. Williams, Acta Metall, 19 (1971) 1153.

[28] H.Y. Kim, H. Hosoda, S. Miyazaki, JIML, 55(2005) 613-617.

[29] J.M. Silcock, Acta Metall, 6(1958)481-92

[30] Y.A. Bagariatskii, G.I. Nosova, Soviet Phys. Cryst.3(1958) 15-26

[31] L.S. Wei, H.Y. Kim, S. Miyazaki, Acta. Mater, 100(2015) 313-322.

[32] M. Tane, T. Nakano, S. Kuramoto, M. Hara, M. Niinomi, N. Takesue, T. Yano, H. Nakajima, Acta Mater. 59 (2011), p. 6975

[33] E.G. Obbard, Y.L. Hao, R.J. Talling, S.J. Li, Y.W. Zhang, D. Dye, R. Yang, Acta Mater. 59 (2011), p. 112

[34] H.Y. Kim, L.S. Wei, S. Kobayashi, M. Tahara, S. Miyazaki, Acta Mater. 61 (2013), p. 4874

[35] R.J. Talling, R.J. Dashwood, M. Jackson, D. Dye, Scr. Mater. 60 (2009), p. 1000

[36] J.G. Niu, W.T. Geng, Acta Mater. 81 (2014), p. 194

[37] P. Castany, A. Ramarolahy, F. Prima, P. Laheurte, C. Curfs, T. Gloriant, Acta Mater. 88 (2015), p. 102

[38] Y. Nii, T. Arima, H.Y. Kim, S. Miyazaki, Phys. Rev. B. 82 (2010), p. 214104

[39] M. Tahara, H.Y. Kim, T. Inamura, H. Hosoda, S. Miyazaki, Acta Mater. 59 (2011), p. 6208

[40] M. Tahara, T. Kanaya, H.Y. Kim, T. Inamura, H. Hosoda, S. Acta Mater. 80 (2014), p. 317

[41] T. Furuhara, S. Annaka, Y. Tomio, T. Maki, Mater Sci Eng A, 825 (2006) 438-440.

[42] M. Tahara, H.Y. Kim, H. Hosoda, S. Miyazaki, Funct Mater Lett, 2 (2009), p. 79

[43] M. Tahara, H.Y. Kim, T. Inamura, H. Hosoda, S. Miyazaki, Mater Trans, 50 (2009), p. 2726

[44] M. Tahara, H.Y. Kim, H. Hosoda, T.H. Nam, S. Miyazaki, Mater Sci Eng A, 527 (2010), p. 6844

[45] L.P. Lefebvre, E.Baril, Advanced engineering materials, 10(2008)9.

[46] M. Tane, T. Nakano, S. Kuramoto, M. Niinomi, N. Takesue, H. Nakajima, Acta Mater, 61(2013)139.

[47] T. Saito, T. Furuta, J.H. Hwang, S. Kuramoto, K. Nishino, N. Suzuki. et al. Sci, 300(2003) 464.

[48] S. Kuramoto, T.Furuta, J.H. Hwang, K. Nishino, T. Sato, Mater Sci Eng A 442(2006)454.

[49] T. Furuta, S. Kuramoto, T. J.H. Hwang, K. Nishino, T. Sato, Mater Trans 46(2005)3001.

[50] R.J. Talling, R.J. Dashwood, M. Jackson, D. Dye, Acta Mater. 57 (2009) 1188-1198.

Chapter 2

Effects of oxygen concentration and phase stability on nano-domain structure and thermal expansion behavior of Ti–Nb–Zr–Ta–O alloys

Abstract

In this study, in order to fully elucidate the origin of nano-domain structure and abnormal thermal expansion behavior of Gum metals, the effects of oxygen concentration, β phase stability and cold rolling on the microstructure and thermal expansion properties were investigated in (Ti-*x*Nb-2Zr-0.7Ta)-*y*O (at.%) (*x* = 21-25; *y* = 0.3-1.8) alloys. Normal thermal expansion behaviors with positive linear thermal expansion coefficients were observed in all the annealed alloys irrespective of oxygen and Nb concentrations. The thermal expansion behavior of as-rolled alloys was strongly affected by the concentration of oxygen and Nb. A negative thermal expansion coefficient was observed in the as-rolled alloys with lower oxygen and Nb concentrations. The thermal expansion coefficient increased with increasing oxygen and Nb concentrations. The amount of nano-domains increased with increasing oxygen concentration while decreased with increasing Nb concentration. The growth of a preferential nano-domain variant was observed in as-rolled alloys and became more prominent with decreasing oxygen and Nb concentrations. The reverse transformation from the nano-domain structure to the β phase occurred with increasing temperature. Thermal expansion behavior of as-rolled alloys resulted from a competing relationship between the contribution of lattice distortion of nano-domain structure and the contribution of lattice vibration of the β phase.

2.1 Introduction

In recent years, Gum metals with a typical composition of Ti-23Nb-2Zr-0.7Ta-1.2O have been studied extensively due to their unusual mechanical and physical properties such as nonlinear elasticity, high strength, low elastic modulus, superplasticity, and Invar-like behavior upon a wide temperature range [1-13, 16]. These unique characteristics have made Gum metals attractive candidates for a wide range of applications such as eyeglass frames, medical equipment, artificial bones, and sporting goods [1, 5, 12, and 13]. It has been recognized that the addition of oxygen plays a crucial role in achieving their unique properties [13–16, 18–20]; however the underlying mechanism of unique properties of Gum metals is still a subject of debate. Tane et al. [13] investigated the influence of oxygen on microstructure and elastic modulus, and claimed that the low Young's modulus of Gum metals is due to the higher concentration of oxygen which suppresses the formation of α'' martensite and ω phases. The plastic deformation mechanism is also affected by the oxygen addition [8]. Besse et al. [9] reported that the addition of oxygen suppresses not only stress induced martensitic transformation but also deformation twinning. Recently, Kim et al. [16] reported the presence of martensite-like nano-domains in Gum metals through systematic transmission electron microscopy experiments. They demonstrated that the nano-domain structure is introduced to release the local stress field induced by interstitial oxygen atoms and the suppression of long-range martensitic transformation in Gum metals is due to the presence of the multi-variant nano-domain structure. They also revealed that the invar-like behavior of Gum metals can be explained by the nano-domain structure. However, the effects of oxygen concentration on the nano-domain structure and thermal expansion behavior have not yet been investigated. Furthermore, the effect of β stability of Gum metals on the nanodomain structure and thermal expansion behavior has not been investigated although the β stability plays an important role on the

formation of the nano-domain structure.

In this study, in order to fully elucidate the origin of invar-like behavior of Gum metals, the effects of oxygen concentration, β phase stability and cold rolling on the nano-domain structure and thermal expansion properties were investigated. The as-rolled and annealed specimens of (Ti-*x*Nb-2Zr-0.7Ta)-*y*O (at.%) (*x* = 21, 23, 25; *y* = 0.3, 0.6, 1.2, 1.5, 1.8) alloys, where the Nb content was varied to prepare alloys with different β phase stability, were processed and their thermal expansion curves were examined. Nano-domain structures of the as-rolled and annealed alloys were investigated by the transmission electron microscopy. The temperature dependence of the lattice parameter of β phase was measured using X-ray diffraction. The origin of abnormal thermal expansion behavior of cold rolled Gum metals was discussed taking into account the influences of oxygen and Nb concentration, cold rolling and thermal vibration of lattice.

2.2 Experimental Procedures

Alloy ingots with nominal compositions of (Ti-*x*Nb-2Zr-0.7Ta)-1.2O (at.%) (*x* = 21, 23, 25) and (Ti-23Nb-2Zr-0.7Ta)-*y*O (at.%)(*y* = 0.3, 0.6, 1.2, 1.5, 1.8) were fabricated by the Ar arc melting method with the pure elemental constituents Ti (99.9%), Nb (99.9%), Zr (99.9%), Ta (99.9%). The oxygen concentration of the alloys was adjusted by the amount of powder TiO_2 (99.9%). Hereafter each alloy is referred to by its oxygen concentration like 0.3O, 0.6O, 1.2O, 1.5O, and 1.8O or Nb concentration like 21Nb, 23Nb, and 25Nb. The ingots were homogenized at 1273 K for 7.2 ks in a vacuum, and then cold rolled up to a 98.5% reduction in thickness. The Nb, Ta, and Zr contents were analyzed using an inductively coupled plasma (ICP) method (iCAP 6500, Thermo Fisher Scientific) and the O and N concentrations were determined by an inert gas fusion-infrared absorption method and fusion-thermal conductivity method (TC600, LECO), respectively.

The chemical compositions of all the alloys are listed in Table 2-1. The differences between the nominal (targeted) compositions and analyzed compositions of substitutional alloying elements were very small; less than 0.4 at.% for Nb, 0.05 at.% for Zr, and 0.04 at.% for Ta, respectively. All alloys exhibited a higher concentration of oxygen about 0.3-0.4 at.% than those of the targeted compositions owing to unavoidable oxygen impurities in raw materials.

Specimens for X-ray diffraction (XRD) measurements and thermal expansion measurements were cut by an electro-discharge machine. One set of specimens was annealing treated at 1023 K for 0.6 ks in an argon atmosphere, followed by water quenching. All the specimens were etched using a solution of H_2O, HNO_3 and HF (5:4:1) in order to remove oxidized surface. Thermal expansion behavior of the specimens with the rolling direction (RD) was characterized by a thermo-mechanical-analyzer (TMA-50, Shimadzu) in the temperature range of 193-353 K with a heating rate of 3 K min^{-1}. The dimensions of the specimens were about 5 mm in gage length, 1.5 mm in width and 0.15 mm in thickness. The XRD analysis was carried out for the as-rolled specimens to detect the structural change with Cu K_α radiation at temperatures between 113 and 393 K. Transmission electron microscopy (TEM) specimens were prepared by a conventional twin-jet polishing machine with a solution of butanol:sulfuric acid (98%):hydrofluoric acid = 93:5:2 by volume at approximately 233 K. TEM observations were conducted with JEOL-2010F apparatus operated at 200 kV.

Table 2-1. Analyzed chemical compositions of Ti-Nb-Zr-Ta-O alloys both in mass% and at.%

	Ti	Nb	Zr	Ta	O	N
(mass%)						
0.3O	Bal.	35.3	3.07	2.13	0.19	0.014
0.6O	Bal.	35.4	3.01	2.09	0.23	0.010
1.2O	Bal.	35.3	3.04	2.04	0.42	0.012
1.5O	Bal.	35.2	2.97	2.09	0.52	0.009
1.8O	Bal.	35.3	2.98	2.14	0.58	0.009
21Nb	Bal.	32.7	3.03	2.16	0.46	0.011
23Nb	Bal.	35.3	3.04	2.04	0.42	0.012
25Nb	Bal.	37.6	2.95	2.10	0.42	0.009
(at.%)						
0.3O	Bal.	22.7	2.01	0.71	0.71	0.060
0.6O	Bal.	22.7	1.97	0.69	0.86	0.042
1.2O	Bal.	22.5	1.98	0.67	1.56	0.050
1.5O	Bal.	22.4	1.92	0.68	1.92	0.038
1.8O	Bal.	22.4	1.93	0.70	2.14	0.038
21Nb	Bal.	20.5	1.94	0.70	1.68	0.046
23Nb	Bal.	22.5	1.98	0.67	1.56	0.050
25Nb	Bal.	24.3	1.94	0.70	1.58	0.039

2.3 Results and discussion

2.3.1 Thermal expansion behavior

Fig. 2-1 shows thermal expansion curves of annealed and as-rolled specimens of 0.3~1.8O alloys and 21~25Nb alloys in the rolling direction. All of the annealed alloys show ordinary positive thermal expansion behavior like a conventional metal irrespective of oxygen concentration or Nb concentration (Fig. 2-1a and c). On the other hand, thermal expansion curves of as-rolled alloys are found to be sensitive with not only the oxygen concentration but also the Nb concentration as shown in Fig. 2-1b and d. Negative thermal expansion behavior was observed in the 0.3O and 0.6O alloys. For the 1.2~1.8O alloys, invar-like behavior which exhibits low linear thermal expansion coefficient was observed as shown in Fig. 2-1b. Negative thermal expansion behavior was observed in the 21Nb alloy while positive thermal expansion behavior which is similar to annealed alloys was observed in the 25Nb alloy. The average linear thermal expansion coefficients in the temperature range of 193~353 K for annealed and as-rolled alloys are plotted as a function of oxygen concentration in Fig. 2-2a and Nb concentration in Fig. 2-2b, respectively. The average linear thermal expansion coefficients of all the annealed alloys show similar values, i.e. in the range of 7.1~8.0 $\times$ 10^{-6} K^{-1}. On the other hand, the as-rolled 0.3O alloy exhibits a lager negative linear expansion coefficient of about -18.0 $\times$ 10^{-6} K^{-1}. The average linear thermal expansion coefficient increased with increasing oxygen concentration and became almost zero when the oxygen concentration is 1.2 at.%. It is noted that the average linear thermal expansion coefficient slightly increased with further increasing oxygen concentration for the 1.2~1.8O alloys as shown in Fig. 2-2(a). The as-rolled 21Nb alloy exhibited a negative linear expansion coefficient of about -7.0 $\times$ 10^{-6} K^{-1} The average linear thermal expansion coefficient increased with

increasing Nb concentration and became close to the value of annealed alloys when the Nb concentration is 25 at.%.

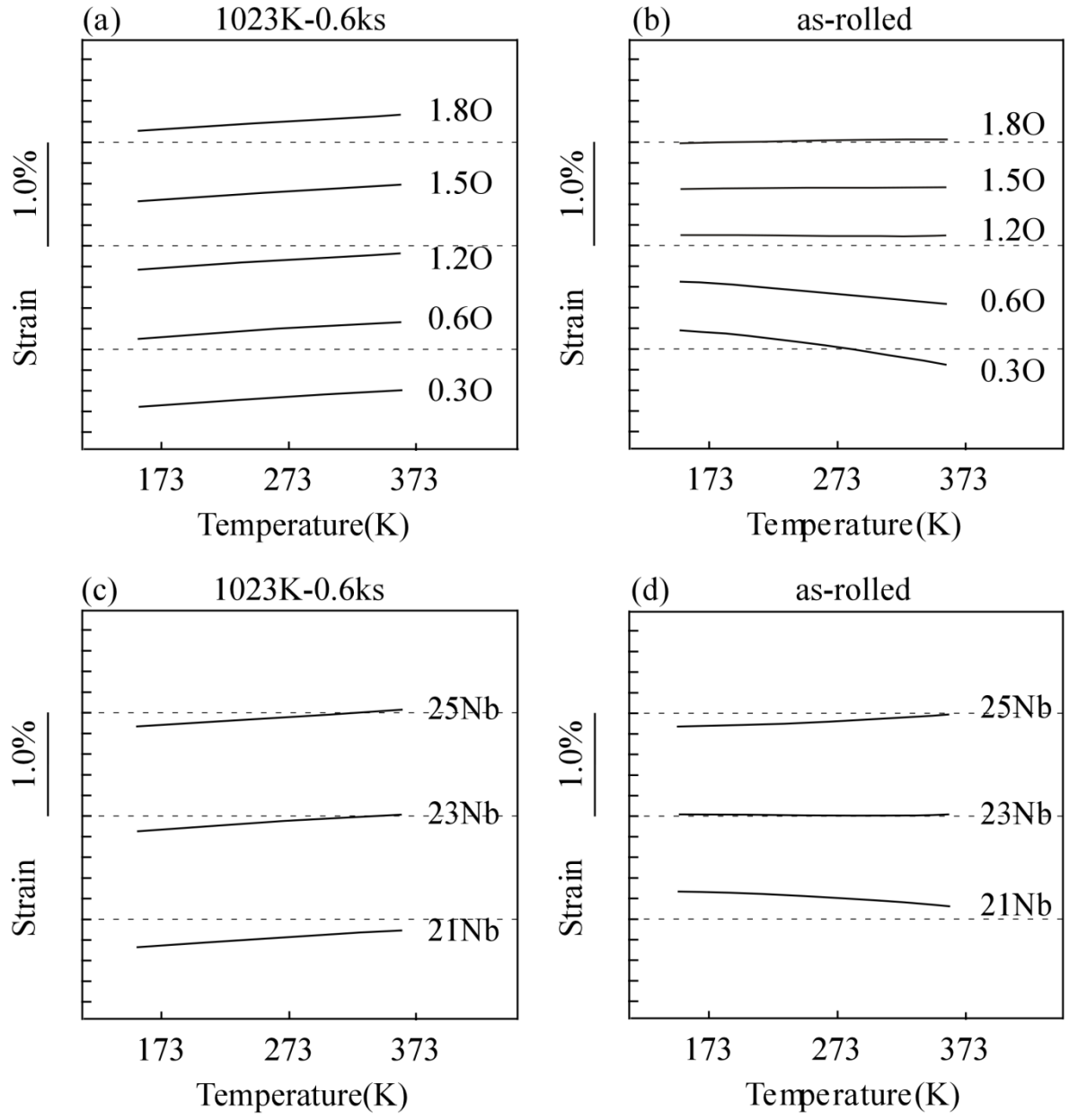

Fig. 2-1. Thermal expansion curves of the annealed and as-rolled alloys.

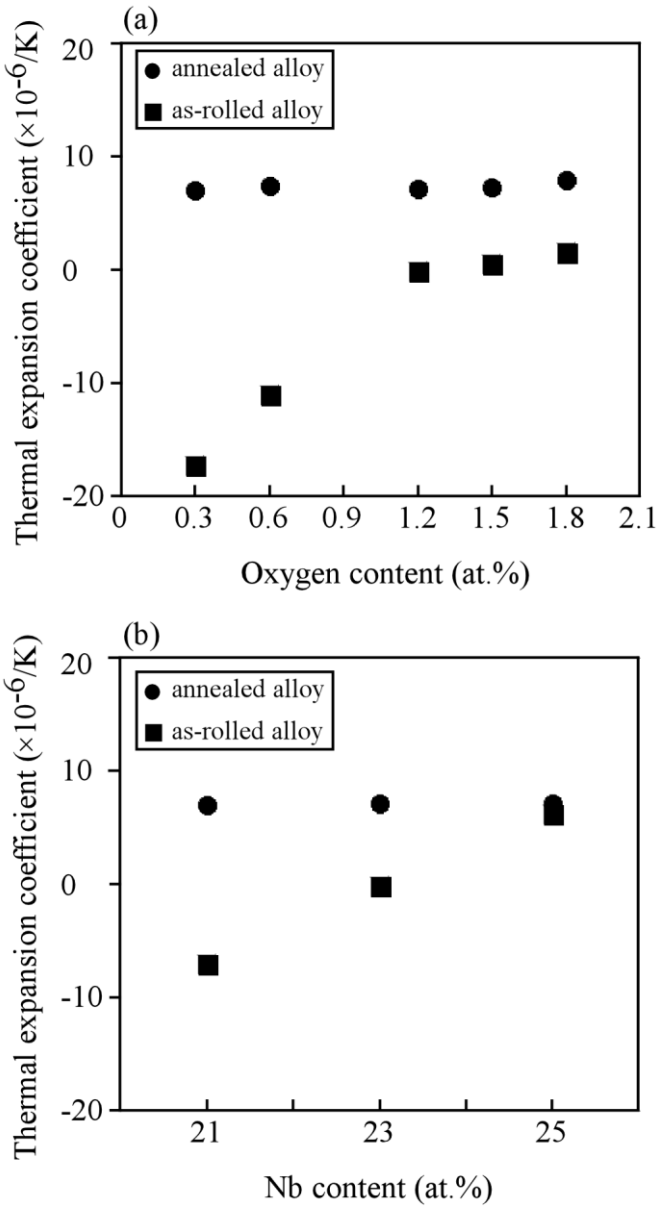

Fig. 2-2. Average linear thermal expansion coefficients of the annealed and as-rolled alloys plotted as a function of (a) oxygen content and (b) Nb content.

2.3.2 Nano-domain structure in annealed and as-rolled 0.3~1.8O alloys

In order to clarify the effect of oxygen concentration on nano-domain structure, TEM analysis was carried out for the annealed and as-rolled specimens of 0.3~1.8O alloys. Fig. 2-3 shows selected area diffraction (SAD) patterns of 0.3~1.8O annealed alloys with the zone axis of $[001]_\beta$. In all alloys, diffuse streaks along the $[\bar{1}10]^*_\beta$ and $[110]^*_\beta$ directions with the intensity maxima at the 1/2 positions can be seen around the fundamental spots of the β phase. Similar domain structure also has been found in Ti-Ni based alloys [17]. It is also seen that the intensity of diffuse streaks increased with increasing oxygen concentration. As reported in our previous papers [16, 21-23], these diffuse streaks are due to a $\{110\}_\beta\langle 1\bar{1}0\rangle_\beta$ type transverse lattice modulation which is crystallographically equivalent to the shuffling mode upon martensitic transformation from the β phase to α″ phase. It has been also confirmed that the modulation mode can be divided into six variants which correspond to six equivalent variants of the α″ martensite phase. The $[\bar{1}10]^*_\beta$ and $[110]^*_\beta$ streaks with intensity maxima at 1/2 positions correspond to shuffling modes $(\bar{1}10)[110]$ and $(110)[\bar{1}10]$, i.e. shuffling modes V5 and V6, respectively, where the same variant numbers for the β-α″ martensitic transformation as in our previous reports [16, 21-23] are used. It is noticed in Fig. 2-3 that the difference of intensity between two diffuse streaks of the $[\bar{1}10]^*_\beta$ and $[110]^*_\beta$ is small, which is consistent with previous reports that six variants of lattice modulation are distributed equivalently in the β phase in the annealed condition.

The dark filed images obtained using the intensity maxima at the 1/2 positions of the $[\bar{1}10]^*_\beta$ and $[110]^*_\beta$ streaks are also shown in Fig. 2-3. Only faint contrast is seen in the dark field image of the 0.3O alloy. In the dark field images of the 0.6O alloy, nanometer-sized domains (nano-domains) are clearly seen. The amount of nano-domains increases with increasing oxygen concentration. Here it is important to note

that there is no noticeable difference in size and distribution of nano-domains between the two dark-field micrographs in each alloy, confirming that the two variants of nano-domains are distributed equivalently in the β phase of each alloy.

The SAD patterns of the 0.3~1.8O as-rolled alloys with the $[001]_\beta$ zone axis are shown in Fig. 2-4. The diffuse streaks along the $[\bar{1}10]^*_\beta$ and $[110]^*_\beta$ directions with the intensity maxima at the 1/2 positions can also be seen in the as-rolled alloys. However, different from the results of annealed alloys that two types of streaks exhibit similar intensities, the intensities of two types of streaks are not equivalent in the as-rolled alloys. For the 0.3O and 0.6O alloys, distinct superlattice spots are seen at the 1/2 positions of $[110]^*_\beta$ streaks whereas one can see that the intensity is very faint at 1/2 positions of $[\bar{1}10]^*_\beta$ streaks. The intensity of the superlattice spots decreased with increasing O concentration, resulting in that the intensities of two types of streaks became similar to each other. The differences of the intensity profiles between annealed and as-rolled conditions are compared in Fig. 2-5 for the 0.6 and 1.5O alloys. The intensity profiles were taken from rectangular frames of SAD patterns in Fig. 2-3 and Fig. 2-4. Two intensity profiles obtained along the $[\bar{1}10]^*_\beta$ and $[110]^*_\beta$ streaks, corresponding to shuffling modes V5 and V6, respectively, were superimposed for easy comparison. For the annealed conditions of both of the 0.6 and 1.5O alloys, two intensity of maxima at the 1/2 positions between fundamental reflections of the β phase are found to be equivalent, indicating that shuffling modes V5 and V6 distribute equivalently in the β phase. It is also seen that the peak intensity of the 1.5O alloy is slightly stronger than that of the 0.6O alloy. On the other hand, for the as-rolled condition, the intensity profiles show a strong dependence of O concentration. In the 0.6O alloy, the intensity of the peak corresponding to the shuffling mode V6 increased significantly while there was a little increase in the peak corresponding to the shuffling mode V5. In the 1.5O alloy, both peaks increased slightly in intensity after cold rolling. It is also noticed that the peak corresponding to the shuffling mode V6 is slightly stronger than

that corresponding to the shuffling mode V5 in the 1.5O alloy; however the difference between the two peaks is not significant when comparing with the 0.6O alloy.

The dark filed images obtained using the intensity maxima at the 1/2 positions of $[\bar{1}10]^*_\beta$ and $[110]^*_\beta$ streaks, corresponding to shuffling modes V5 and V6, respectively, are also shown in Fig. 2-4. The nano-domains corresponding to the shuffling mode V6 in all as-rolled specimens became clearly visible and their size became larger when comparing with those of the annealed specimens in Fig. 2-3. It is also important to note that the growth of nano-domains was more prominent in the alloys with lower O concentration. On the other hand, there was little change in the nano-domains corresponding to the shuffling mode V5 in all alloys.

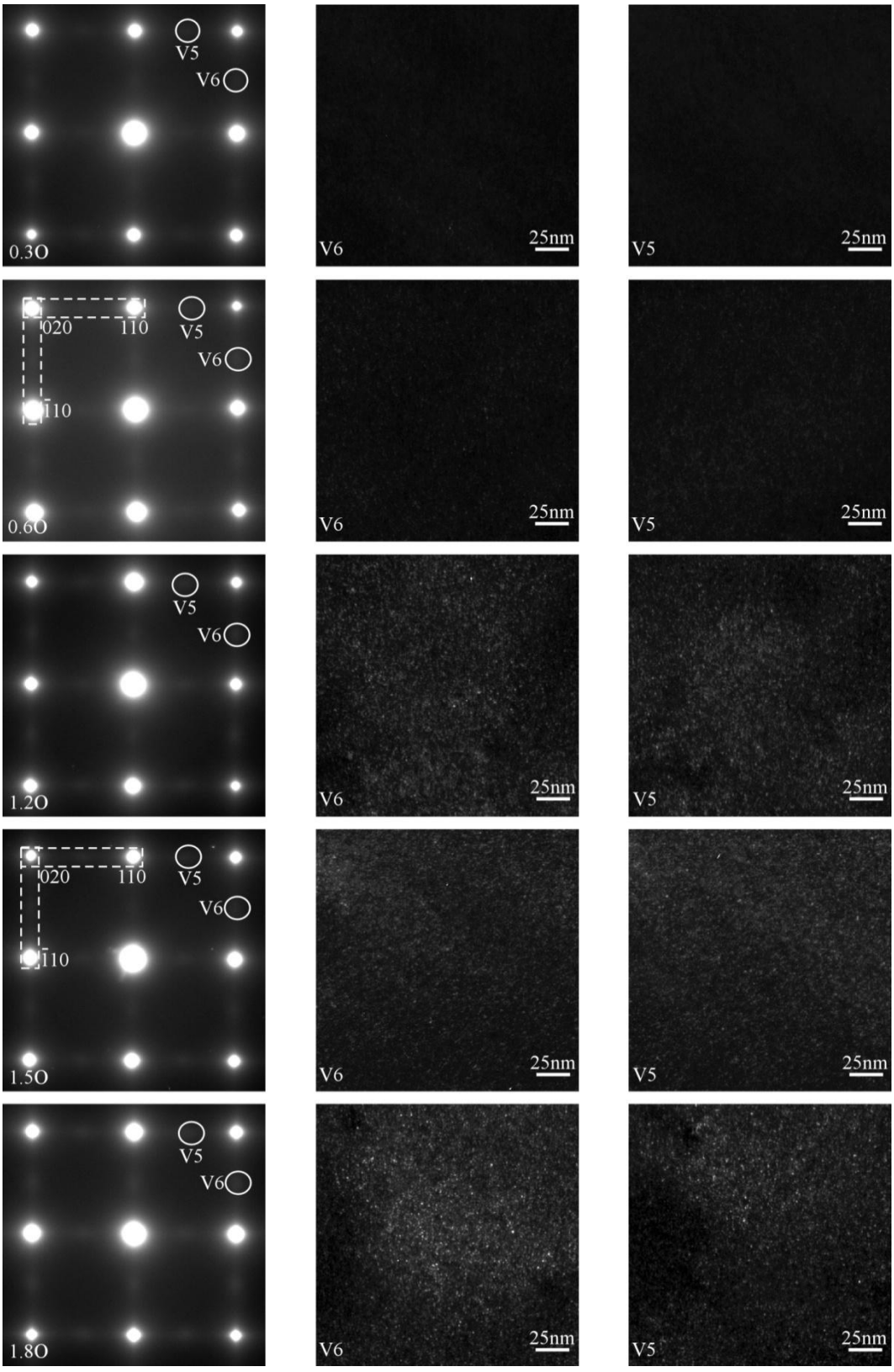

Fig. 2-3. Selected area diffraction patterns and dark field images obtained from intensity maxima at the 1/2 positions of the $[\bar{1}10]^*_\beta$ and $[110]^*_\beta$streaks for annealed 0.3~1.8O alloys.

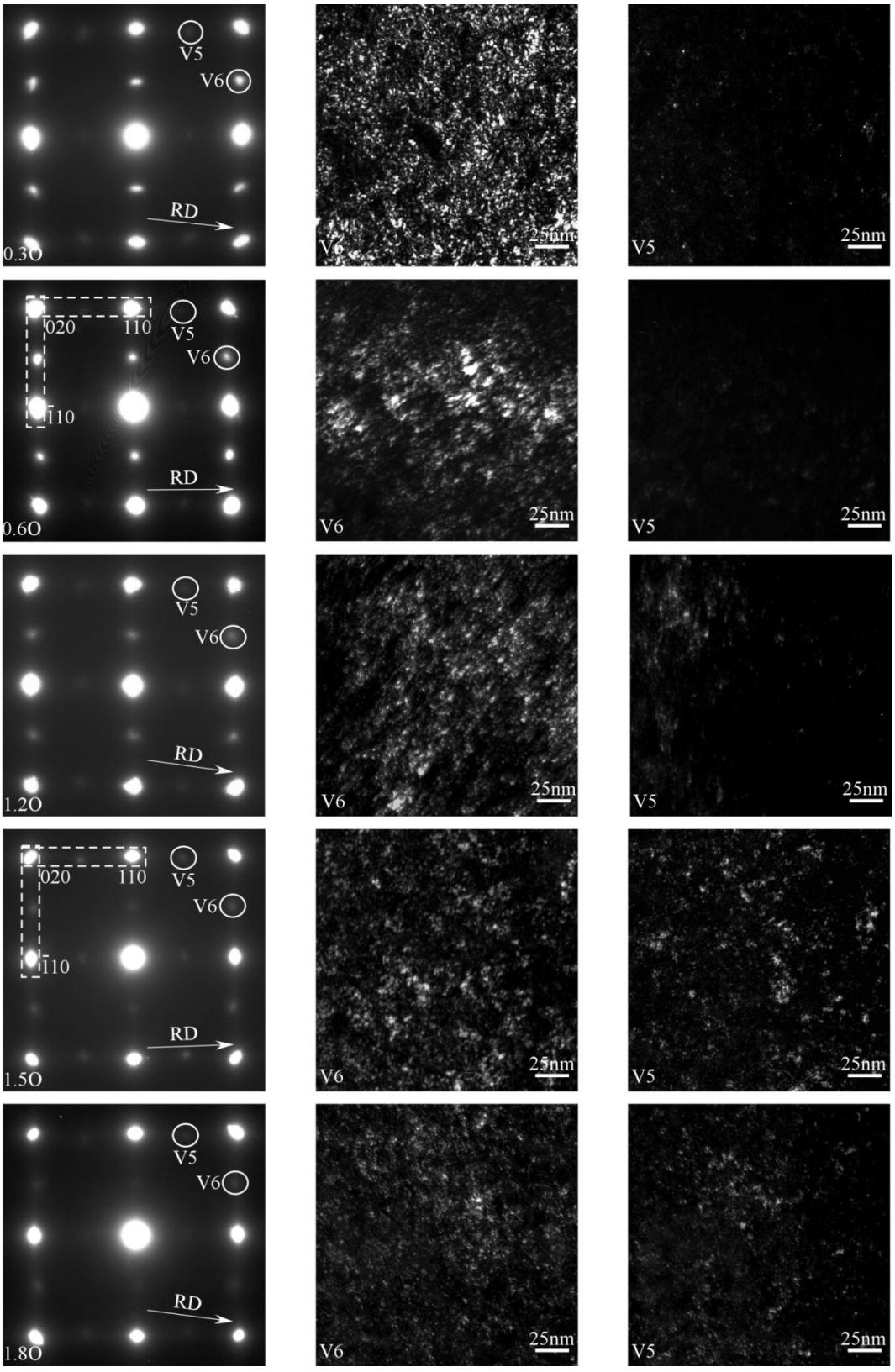

Fig. 2-4. Selected area diffraction patterns and dark field images obtained from intensity maxima at the 1/2 positions of the $[\bar{1}10]^*_\beta$ and $[110]^*_\beta$streaks for as-rolled 0.3~1.8O alloys.

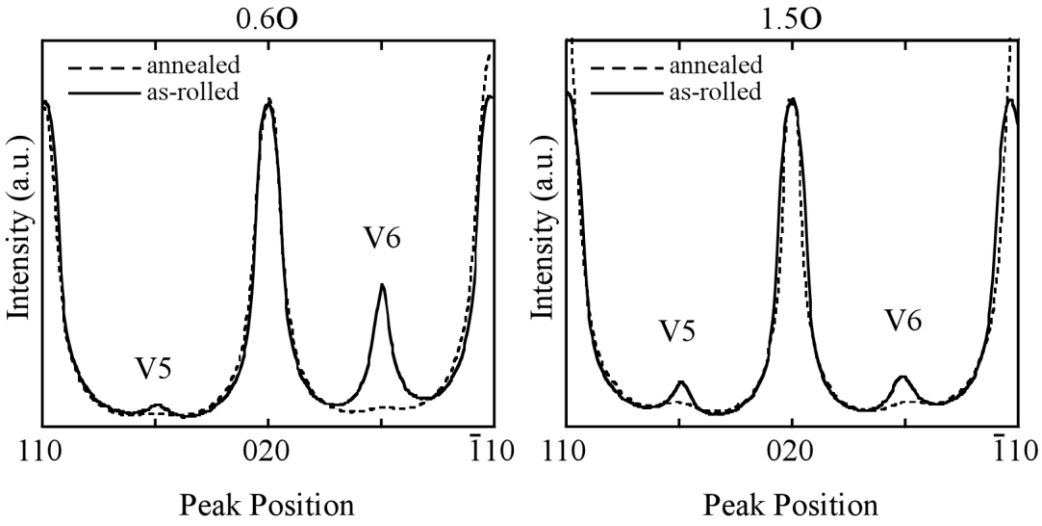

Fig. 2-5. Comparison of the intensity profiles of the $[\bar{1}10]^*_\beta$ and $[110]^*_\beta$ streaks taken from rectangular frames of SAD patterns in Fig. 2-3 and 2-4 for 0.6O and 1.5O alloys.

2.3.3 Nano-domain structure in annealed and as-rolled 21~25Nb alloys

TEM investigation were also carried out on specimens of 21~25Nb alloys with the oxygen concentration of 1.2 at.%, in order to investigate the effect of the β phase stability on the nano-domain structure. Fig. 2-6 shows selected area diffraction (SAD) patterns of 21~25Nb annealed alloys with the zone axis of $[001]_\beta$. It is seen that the diffuse streaks along the $[\bar{1}10]^*_\beta$ and $[110]^*_\beta$ directions with the intensity maxima at the 1/2 positions are present around the fundamental spots of the β phase. The intensity of diffuse streaks decreased with increasing Nb concentration. The dark filed images obtained using the intensity maxima at the 1/2 positions of the $[\bar{1}10]^*_\beta$ (V5) and $[110]^*_\beta$ (V6) streaks are also shown in Fig. 2-6. The nano-domains distributed in the dark field images of the 21Nb alloy are visible clearly. It can also be noticed that no discernible difference in size and distribution of nano-domains between the two dark field images. The

amount of nano-domains decreases with increasing Nb concentration, and no clear image of nano-domains was obtained in the 25Nb alloys.

Fig. 2-7 shows SAD patterns and dark field images of the 21~25Nb as-rolled alloys with the $[001]_{\beta}$ zone axis. Similarly to the results of Fig. 2-4, the intensities of two types of streaks are not equivalent in the as-rolled alloys differently from the results of annealed alloys. The changes of the intensities of two types of streaks and corresponding nano-domains are essentially the same as those in the 0.3~1.8O alloys. The superlattice spots and nano-domains corresponding to the shuffling mode V6 in the 21Nb alloy became more distinct and clear whereas those corresponding to the shuffling mode V5 are faint and unclear even after cold rolling. The intensity of the superlattice spots corresponding to the shuffling mode V6 decreased with increasing Nb concentration, and no noticeable difference between both the shuffling modes was observed in the 25Nb alloy as shown in Fig 2-8. It is also noted that there was little change in the intensity of the superlattice spots and nano-domains corresponding to the shuffling mode V5 in all alloys.

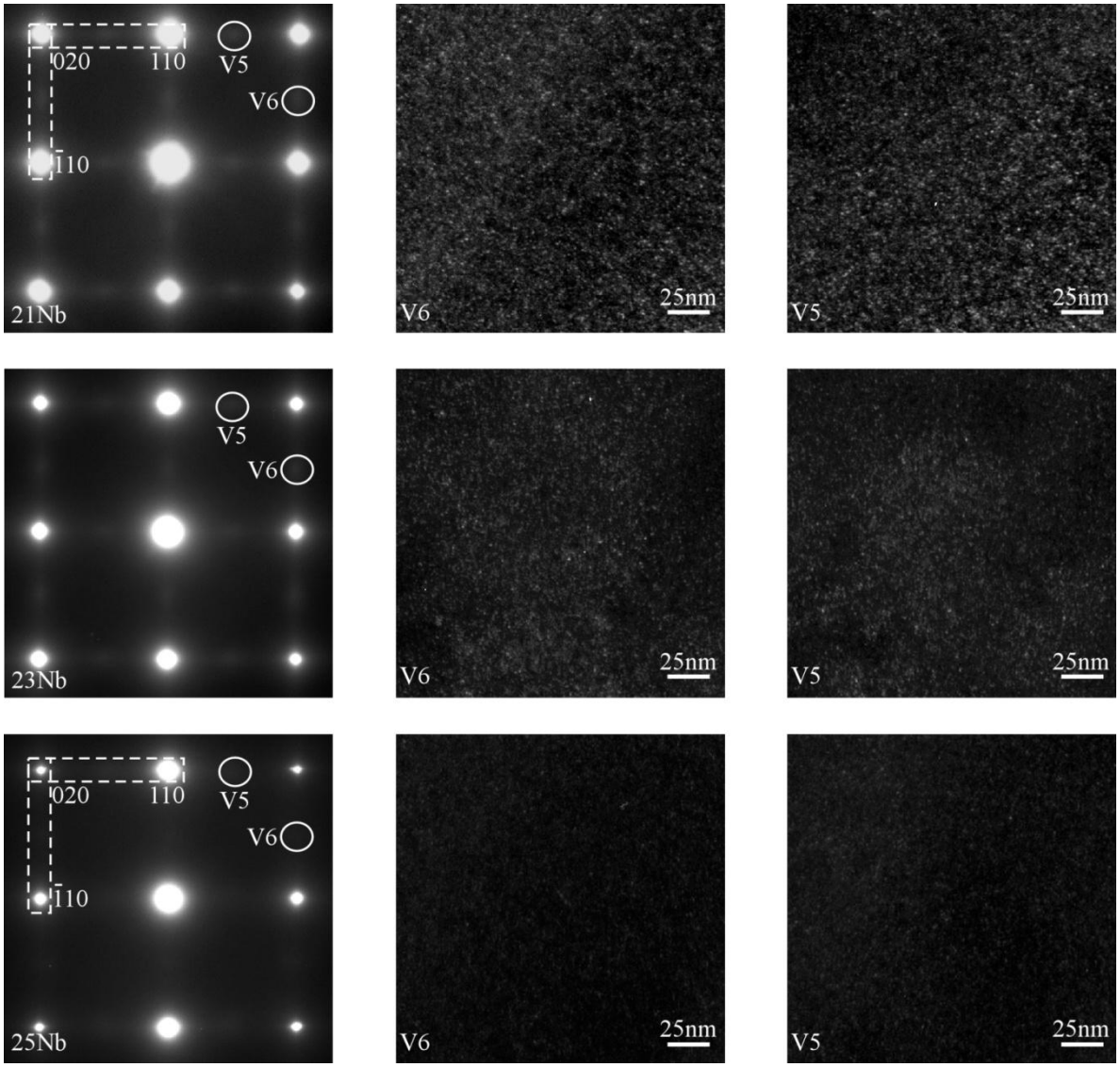

Fig. 2-6. Selected area diffraction patterns and dark field images obtained from intensity maxima at the 1/2 positions of the $[\bar{1}10]^*_\beta$ and $[110]^*_\beta$ streaks for annealed 21~25Nb alloys.

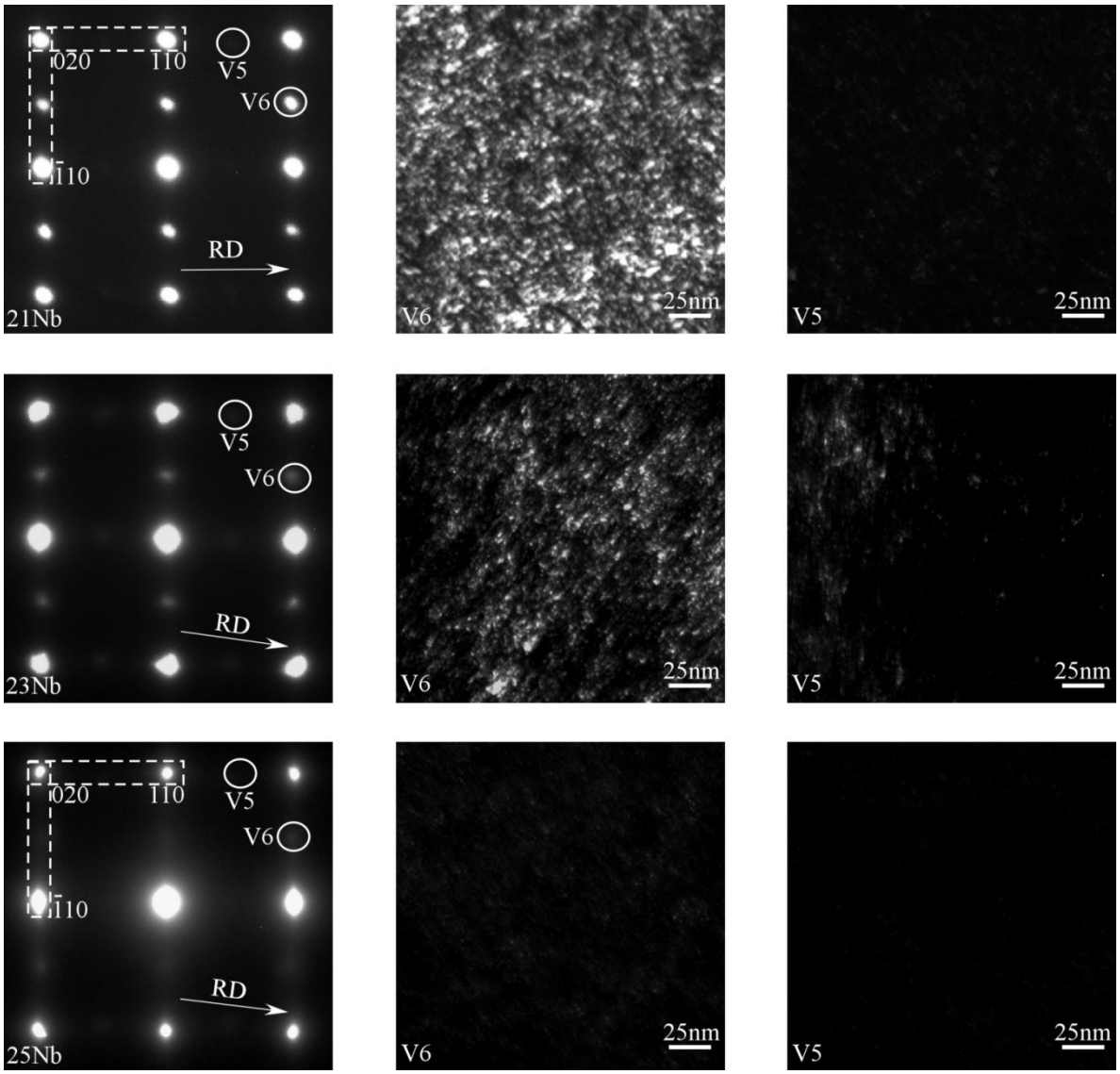

Fig. 2-7. Selected area diffraction patterns and dark field images obtained from intensity maxima at the 1/2 positions of the $[\bar{1}10]^*_\beta$ and $[110]^*_\beta$ streaks for as-rolled 21~25Nb alloys.

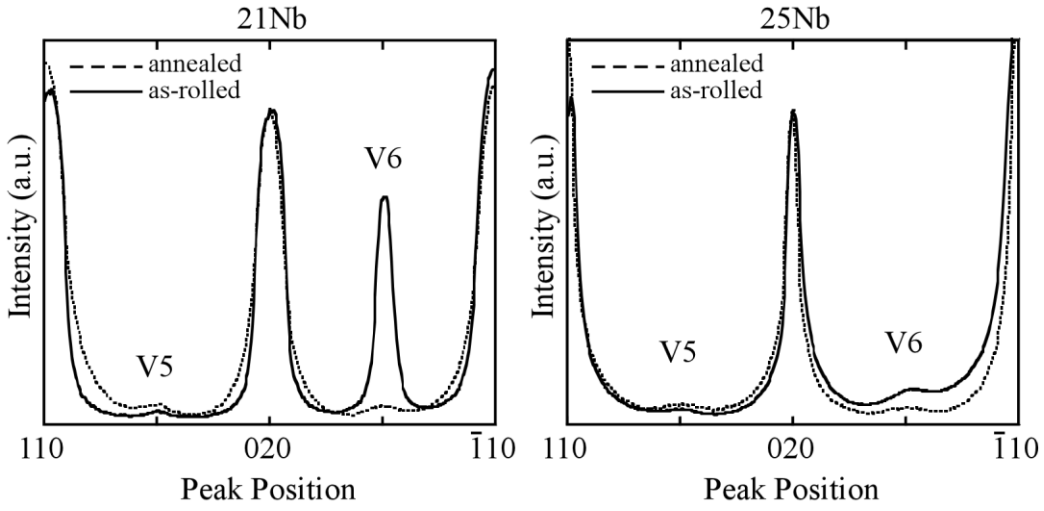

Fig. 2-8. Comparison of the intensity profiles of the $[\bar{1}10]^*_\beta$ and $[110]^*_\beta$ streaks taken from rectangular frames of SAD patterns in Fig. 2-6 and 2-7 for 21Nb and 25Nb alloys.

2.3.4 XRD analysis

In situ XRD profiles were obtained between 113 K and 393 K for the as-rolled specimens of the 0.3~1.8O alloys within a 2θ range from 52^o to 62^o, and the results are shown in Fig. 2-9. The first XRD profile was obtained at 113 K, and the following measurements were carried out after increasing the temperature by 40 K for entire tests in each specimen. In the XRD profile of the 0.3O alloy obtained at 113 K (Fig. 2-9a), a broad peak appears as a shoulder on the right side of 200_β peak. It is considered that the broad peak is associated with the nano-domain structure. The broad peak became weaker with increasing test temperature, suggesting that the reverse transformation from the nano-domain structure to β occurred gradually. It is also noted that the 200_β peak is still asymmetrical at 393 K. In the XRD profiles of the 0.6O

alloy shown in Fig. 2-9b, a broad peak was also observed on the right side of the 200_β peak although it was not distinct when compared with the 0.3O alloy. In the case of the 1.2O and 1.8O alloys (Fig. 2-9c and d), the diffuse peak became difficult to be distinguished from the 200_β peak, indicating that the growth of favorable nano-domain variant was suppressed in the alloys with a higher oxygen concentration which is consistent with the TEM results as shown in Fig. 2-4. However it is seen that the 200_β peak became sharper and more symmetrical gradually with increasing test temperature.

It is also important to note that the 200_β peak shifted toward a lower 2θ value with increasing test temperature in all alloys, implying that the lattice constant of the β phase increased with temperature. The relative changes in the lattice constant of the β phase are plotted in Fig. 2-10 as a function of test temperature for as-rolled specimens of the 0.3~1.8O alloys. It is clearly seen that the lattice constant of the β phase increased almost linearly with similar slopes of about 8.34×10^{-6} K^{-1}, although there are some scatter, as temperature increased in all alloys. This result suggests that the contributions of the phonons (thermal vibration of lattice) to thermal expansion are similar in the 0.3~1.8O alloys, and also that not only the negative thermal expansion behavior in 0.3~0.6O alloys but also invar-like behavior in 1.2~1.5O are not due to the thermal expansion of the β phase.

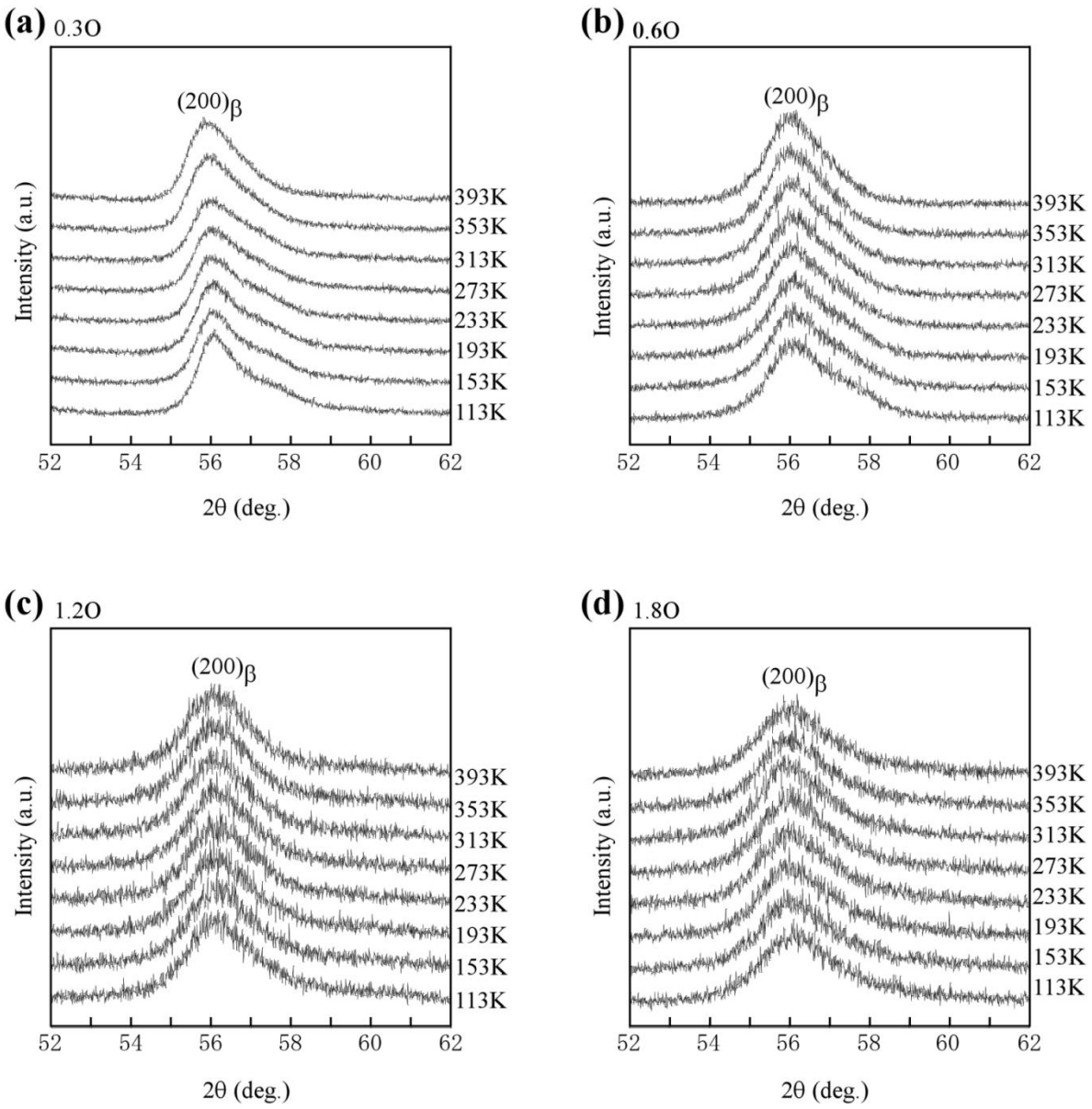

Fig. 2-9. In situ XRD profile obtained between 113~393K for the as-rolled specimens of the 0.3-1.8O alloys within the 2θ range of 52^{o} and 62^{o}.

Similar in-situ XRD measurements were carried out for the 21~23Nb alloys and the results are shown in Fig. 2-11. In the XRD profile of the 21Nb alloy obtained at 113 K two broad peaks were observed partially overlapped each other: the left peak is corresponding to the 200_{β} peak while the right peak is due to the

nano-domain of the favorable variant. It is seen that the intensity of the right peak decrease with increasing temperature, indicating that the reverse transformation from the nano-domain to the β phase occurred. The peak from the nano-domains becomes progressively more difficult to resolve in the 25Nb alloy, which is consistent with the results of TEM analysis as shown in Fig. 2-7. It is also noted that XRD profiles of the 25Nb alloys showed no significant change with increasing temperature. These results imply that the formation and growth of nano-domain variants were relatively suppressed with increasing Nb content, i.e. stability of β phase. Fig. 2-12 shows the relative changes in the lattice constant of the β phase as a function of test temperature for as-rolled specimens of the 21~25Nb alloys. It is seen that the lattice constant of the β phase increased monotonically with similar slopes with increasing test temperature in all alloys, indicating that the contributions of the lattice vibration of the β phase to thermal expansion behavior are similar irrespectively of nano-domains.

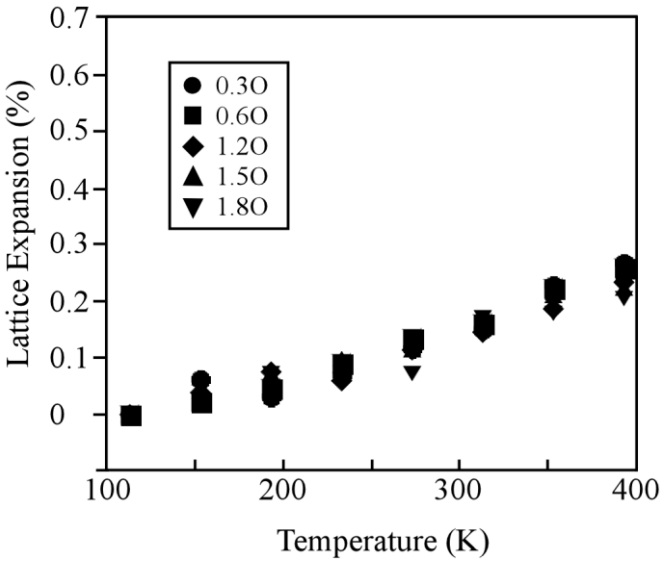

Fig. 2-10. The relative changes in the lattice constant of the β phase as a function of test temperature for as-rolled specimens of the 0.3~1.8O alloys.

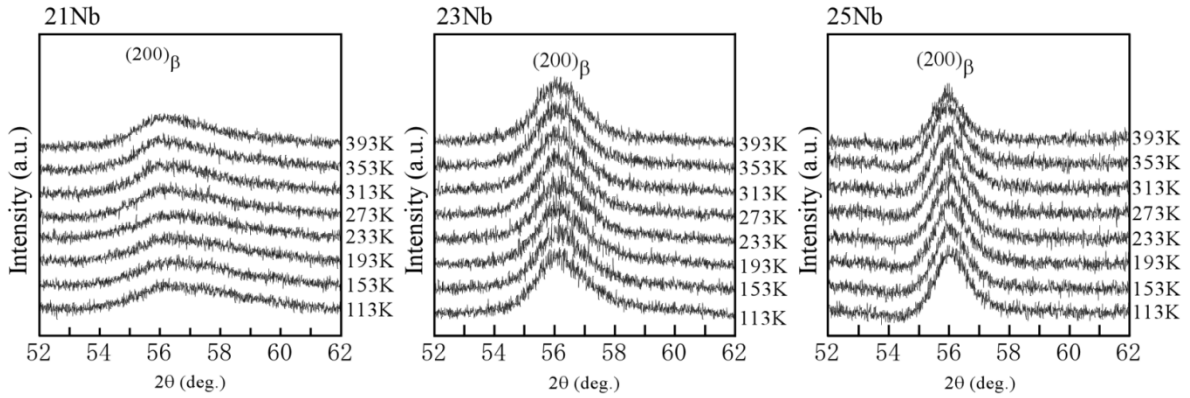

Fig. 2-11. In situ XRD profiles obtained between 113 K and 393 K for the as-rolled specimens of the 21~25Nb alloys within the 2θ range of 52^{o} and 62^{o}.

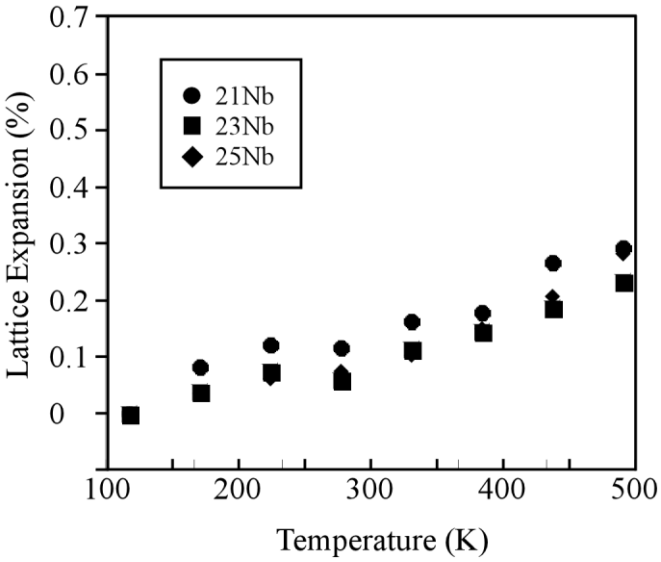

Fig. 2-12. The relative changes in the lattice constant of the β phase as a function of test temperature for as-rolled specimens of the 21~25Nb alloys.

2.3.5. Mechanism of anomalous thermal expansion behavior

It is proposed that thermal expansion behavior of the Ti-Nb-2Zr-0.7Ta-O alloys is determined by two factors, i.e. thermal vibration of the lattice and lattice distortion strain of nano-domains. XRD and TEM analyses exhibited that the contribution of lattice distortion strain of nano-domains is significantly influenced by the stress state, oxygen and Nb concentration. The corresponding schematic illustrations are shown in Fig. 2-13 and Fig. 2-14. In Fig. 2-13, there is no preferential growth of a specific nano-domain variant in the annealed specimens although the amount of nano-domains increased with increasing oxygen concentration shown in Fig. 2-13 (a) and (b) or decreasing Nb concentration as shown in Fig. 2-3 and Fig. 2-6. This means that the contribution of thermal vibration of lattice is dominating in the annealed specimens, resulting in normal positive thermal expansion behavior with similar linear thermal expansion coefficients.

In the as-rolled specimens, as shown in Fig. 2-13 (c) and (d) and Fig. 2-14, the concentrations of oxygen and Nb significantly affect the amount of lattice distortion strain of nano-domains. The lattice distortion strain decreases as the oxygen concentration increases because the growth of favorable domains becomes harder due to mutual suppression effect of nano-domains, as shown in Fig. 2-4 and Fig. 2-10, resulting in changing thermal expansion coefficient from negative to zero. It is also apparent from Fig. 2-10 that the growth of nano-domains is second-order like transformation: the lattice distortion strain changes continuously with increasing temperature. Similar transformation was also observed in other alloys [20, 23-25]. Thus, it is expected that the magnitude of lattice distortion strain caused by the formation of one nano-domain is strongly affected by the stress state, temperature and interaction between other nano-domains. On the other hand, it should be noted that there are no distinct differences in the contribution of thermal vibration of lattice for the as-rolled alloys as shown in Fig. 2-10. These results suggest that the negative thermal expansion behavior in the as-rolled 0.3O and 0.6O alloys is due to the fact that the lattice distortion strain component of nano-domains is larger than the thermal vibration component. The contribution of the lattice distortion strain of nano-domains decreases with increasing oxygen concentration due to the increased local barriers, and becomes smaller than that of the thermal vibration of lattice, explaining a small positive thermal expansion coefficient in the 1.8O alloy. It is proposed that the positive strain due to the thermal vibration of the lattice compensates the negative strain due to the lattice distortion of the nano-domains, resulting in invar-like behavior in 1.2~1.5O alloys shown in Fig. 2-15.

The concentration of Nb also affects the formation of nano-domains and lattice distortion strain of the nano-domains. As the Nb concentration decreases the β phase becomes unstable [26, 27], leading to not only an easier formation of nano-domains but also an easier growth of the favorable nano-domain variants during cold rolling (Fig. 2-14). XRD analysis shown in Fig. 2-11 indicates that the lattice distortion strain of

nano-domains increased with decreasing Nb content. As a result the negative thermal expansion coefficient upon heating in the 21Nb alloy is due to the reverse transformation of nano-domains which causes a negative strain larger than thermal vibration strain. In conclusion, it is suggested that the amount of lattice distortion strain of nano-domains which is governed by the concentration of oxygen and the stability of β phase, determines the thermal expansion behavior of Ti-Nb-2Zr-0.7Ta-O alloys.

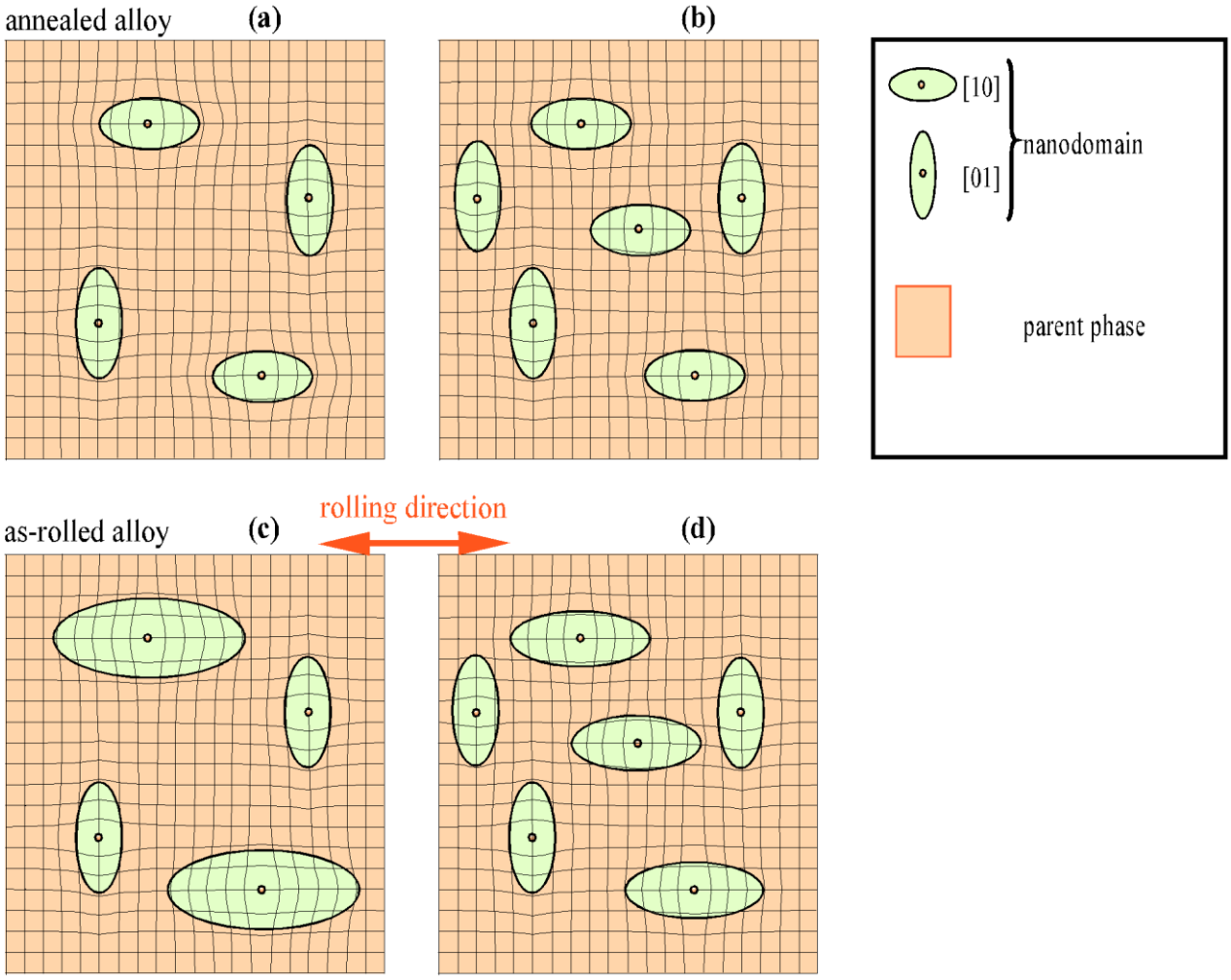

Fig. 2-13. The schematic illustration for the change of two nano-domain variants with increasing oxygen concentration for annealed alloys in (a) and (b) and as-rolled alloys in (c) and (d).

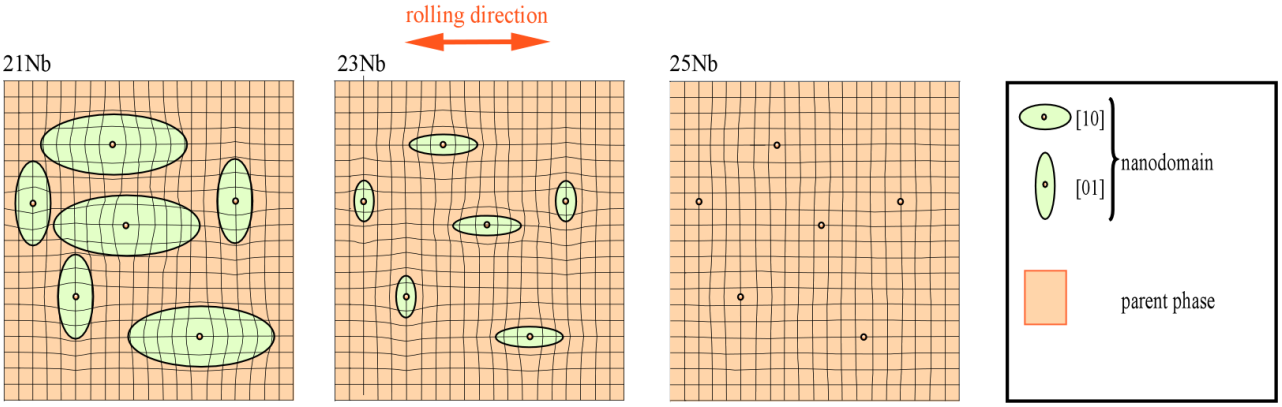

Fig. 2-14. The schematic illustration for the change of two nano-domain variants with increasing Nb concentration for as-rolled alloys.

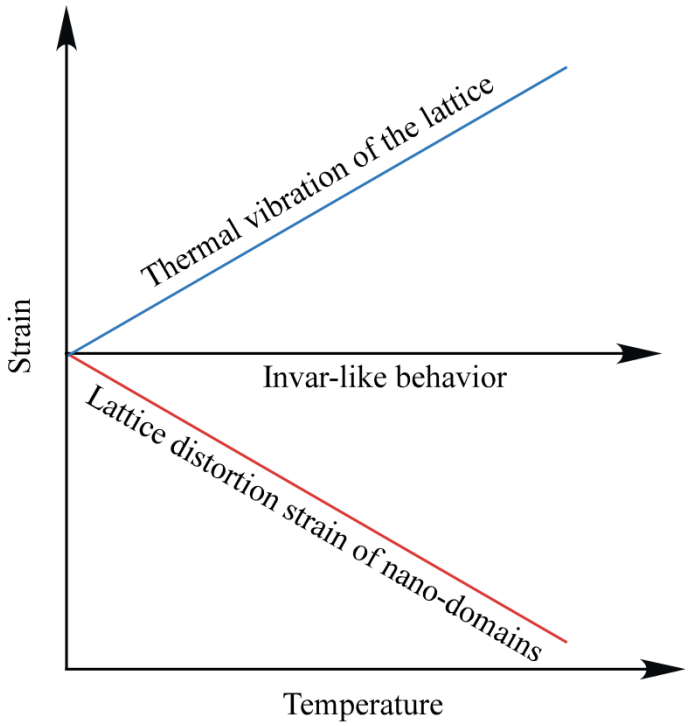

Fig. 2-15. The schematic illustration for invar-like behavior in 1.2~1.5O as-rolled alloys.

2.4. Conclusions

In this study, the effects of oxygen concentration, β phase stability and cold rolling on the nano-domain structure and thermal expansion properties of (Ti-*x*Nb-2Zr-0.7Ta)-*y*O (at %) (*x*=21, 23, 25; *y*=0.3, 0.6, 1.2, 1.5, 1.8) alloys were investigated in detail by TMA, TEM and *in situ* XRD. The results are summarized as follows.

1. Normal positive thermal expansion behaviors with similar linear thermal expansion coefficients were obtained in all the annealed alloys irrespective of oxygen and Nb concentrations. In the alloys with 23at.%Nb, the as-rolled 0.3O alloy exhibited a lager negative linear expansion coefficient and the linear thermal expansion coefficient increased with increasing oxygen concentration, and then became almost zero when the oxygen concentration was 1.2 at.% showing invar-like behavior. When the oxygen content was 1.2at.%, the as-rolled 21Nb alloy exhibited a negative linear expansion coefficient and the linear thermal expansion coefficient increased with increasing Nb concentration and became close to the value of annealed alloys when the Nb concentration was 25 at.%.
2. The amount of nano-domains increased with increasing oxygen concentration while decreased with increasing Nb concentration. The growth of a preferential nano-domain variant occurred in as-rolled alloys. The growth of nano-domains became more prominent in the as-rolled alloys as the oxygen and Nb content decreased.
3. A broad peak which associated with the nano-domain structure appeared as a shoulder on the right side of 200_{β} peak and it became weaker with increasing test temperature due to the reverse transformation from the nano-domain structure to β phase. With increasing oxygen or Nb concentration, the diffuse peak became difficult to be distinguished from the 200_{β} peak.

4. The lattice constant of the β phase increased monotonically with similar slopes with increasing test temperature in all alloys, indicating that the contributions of thermal vibration of lattice to thermal expansion behavior are similar. Thermal expansion behavior was determined by the amount of lattice distortion strain of nano-domains which increased with decreasing oxygen concentration or stability of β phase.

References

[1] T. Saito, T. Furuta, J.H. Hwang, S. Kuramoto, K. Nishino, N. Suzuki, R. Chen, A.Yamada, K. Ito, Y. Seno, T. Nonaka, H. Ikehata, N. Nagasako, C. Iwamoto, Y. Ikuhara, T. Sakuma, Sci. 300 (2003) 464-467.

[2] M.Y. Gutkin, T. Ishizaki, S. Kuramoto, I.A. Ovid'ko, Acta Mater. 54 (2006) 2489-2499.

[3] T. Li, J.W. Morris, N. Nagasako, S. Kuramoto, D.C. Chrzan, Phys. Rev. Lett. 98 (2007) 105503.

[4] H. Xing, J. Sun, Q. Yao, W.Y. Guo, R. Chen, Appl. Phys. Lett. 92 (2008) 151905.

[5] R.J. Talling, R.J. Dashwood, M. Jackson, D. Dye, Acta Mater. 57 (2009) 1188-1198.

[6] E.A. Withey, A.M. Minor, D.C. Chrzan, J.W. Morris Jr, S. Kuramoto, Acta Mater. 58 (2010) 2652-2665.

[7] J.W. Morris Jr, Y. Hanlumyuang, M. Sherburne, E. Withey, D.C. Chrzan, S. Kuramoto, Y. Hayashi, M. Hara, Acta Mater. 58 (2010) 3271-3280.

[8] S. Kuramoto, T. Furuta, J.H. Hwang, K. Nishino, T. Saito, Metall. Mater. Trans. A. 37A (2006) 657-662.

[9] M. Besse, P. Castany, T. Gloriant, Acta Mater. 59 (2011) 5982-5988.

[10] Y. Yang, G.P. Li, G.M. Cheng, Y.L. Li, K. Yang, Appl. Phys. Lett. 94 (2009) 061901.

[11] T. Yano, Y. Murakami, D. Shindo, S. Kuramoto, Acta Mater. 57 (2009) 628-633.

[12] M.Tane, S. Akita, T. Nakano, K. Hagihara, Y. Umakoshi, M. Niinomi, H. Mori, H. Nakajima, Acta Mater. 58 (2010) 6790-6798.

[13] M. Tane, T. Nakano, S. Kuramoto, M. Hara, M. Niinomi, N. Takesue, T. Yano, H. Nakajima, Acta Mater. 59 (2011) 6975-6988.

[14] J.I. Kim, H.Y. Kim, H. Hosoda, S. Miyazaki, Mater. Trans. 46 (2005) 852-857.

[15] E.G. Obbard, Y.L. Hao, R.J. Talling, S.J. Li, Y.W. Zhang, D. Dye, R. Yang, Acta Mater. 59 (2011) 112-125.

[16] H.Y. Kim, L.S. Wei, S. Kobayashi, M. Tahara, S. Miyazaki, Acta Mater. 61 (2013) 4874-4886.

[17] S. Sarkar, X. Ren, K. Otsuka, Phys. Rev. Lett. 95 (2005) 205702.

[18] R.J. Talling, R.J. Dashwood, M. Jackson, D. Dye, Scr. Mater. 60 (2009) 1000-1003.

[19] J.G. Niu, W.T. Geng, Acta Mater. 81 (2014) 194-203.

[20] P. Castany, A. Ramarolahy, F. Prima, P. Laheurte, C. Curfs, T. Gloriant, Acta Mater. 88 (2015) 102-111.

[21] Y. Nii, T. Arima, H.Y. Kim, S. Miyazaki, Phys. Rev. B. 82 (2010) 214104.

[22] M. Tahara, H.Y. Kim, T. Inamura, H. Hosoda, S. Miyazaki, Acta Mater. 59 (2011) 6208-6218.

[23] M. Tahara, T. Kanaya, H.Y. Kim, T. Inamura, H. Hosoda, S. Miyazaki, Acta Mater. 80 (2014) 317-326.

[24] Y. Yang, P. Castany, M. Cornen, F. Prima, S.J. Li, Y.L. Hao, T. Gloriant, Acta Mater. 88 (2015) 25-33.

[25] J.P. Liu, Y.D. Wang, Y.L. Hao, H.L. Wang, Y. Wang, Z.H. Nie, R. Su, D. Wang, Y. Ren, Z.P. Lu, J.G. Wang, X.D. Hui, R. Yang, Acta Mater. 81(2014) 476-486.

[26 H.Y. Kim, H. Satoru, J.I. Kim, H. Hododa, S. Miyazaki, Mater. Trans. 45 (2004) 2443-2448.

[27] H.Y. Kim, Y. Ikehara, J.I. Kim, H. Hosoda, S. Miyazaki, Acta Mater. 54 (2006) 2419-2429.

Chapter 3

Effects of temperature and oxygen addition on mechanical behavior of Ti-Nb-Zr-Ta-O alloys

Abstract

The microstructure and the deformation behavior of Ti-23Nb-2Zr-0.7Ta-*x*O (at %) (*x*=0.3, 0.6, 1.2, 1.5, 1.8) were investigated. The stress induced martensitic transformation was suppressed with increasing oxygen concentration, resulting in narrow stress hysteresis in stress-strain curves of the alloys with higher oxygen concentration. In the 0.3~0.6O alloys, the apparent yielding stress decreased with decreasing test temperature at higher temperatures, but the yielding stress increased with decreasing test temperature at lower temperature region. The abnormal increase in the yielding stress is due to the formation of athermal ω phase. Oxygen suppressed the formation of the athermal ω phase. In the alloys with higher oxygen concentration (1.2~1.8O alloys), the apparent yielding stress decreased linearly with decreasing test temperature satisfying Clausius-Clapeyron relationship.

3.1 Introduction

Gum metal possesses several unique properties, such as high strength, a low elastic modulus, non-linear elasticity, super-plasticity, and Invar-like behavior [1-11]. Over the years there have been many researches attempt to elucidate the deformation behavior of Gum metals. Talling et al. [4] investigated the deformation mechanisms of Gum metal using the aid of in situ synchrotron X-ray diffraction and TEM. They

demonstrated that the superelastic behavior of Gum metal can be accountable by reversible stress induced martensitic transformation and higher oxygen content can raise the triggering stress for the martensitic transformation. Tane et al.[8] investigated the low Young's modulus of Gum metal with varies oxygen concentration and the effect of cold working. They showed that high oxygen concentration can suppress the martensitic transformation and ω phase, resulting in low Young's modulus. As reported in our previous papers [10-13], the oxygen can occupy octahedral interstitial sites of bcc matrix leading to the local strain field and induced nanosized modulated domain (nano-domain) structure. The nano-domain structure can suppress the long-range martensitic transformation and is deeply affected by the oxygen concentration. It is hence believed that the deformation behavior of Gum metals is related to the martensitic phase transformation. And also it is considered that the nano-domain and oxygen play a crucial role in the deformation mechanism of Gum metals. Despite a thorough investigation, the effect of temperature on the deformation behavior of Gum metals has not been fully elucidated. In this study, the deformation behaviors of the annealed specimens of Ti-23Nb-2Zr-0.7Ta-*x*O (at %) (*x*=0.3, 0.6, 1.2, 1.5, 1.8) were investigated centered on the effects of temperatures, the oxygen concentration and the ω phase.

3.2 Experimental Procedures

Ti-23Nb-2Zr-0.7Ta-*x*O (at %) (*x*=0.3, 0.6, 1.2, 1.5, 1.8) ingots were fabricated by the Ar arc melting method and the oxygen concentration of each alloys was adjusted by the amount of powder TiO_2 (99.9%). Hereafter each alloy is referred to by its oxygen concentration like 0.3O, 0.6O, 1.2O, 1.5O, and 1.8O. Then the ingots were homogenized at 1273 K for 7.2 ks in a vacuum and cold rolled up to a 98.5% reduction in thickness. All the specimens for the measurements were cut by an electro-discharge machine then etched to

remove oxidized surface. The specimens were carried out annealing treatment at 1023 K for 0.6 ks in an argon atmosphere, and followed by water quenching. The deformation behaviors were characterized by a tensile testing machine at temperatures between 193 and 333K. The microstructures were investigated by JEOL-2010F Transmission electron microscopy (TEM) apparatus at 200 kV. The electrical resistivity was carried out between 200 and 300K with a heating rate of 1 K min^{-1}, using the four-point probe method.

3.3 Results and discussion

3.3.1 Transformation behavior

Fig. 3-1 shows stress-strain curves obtained at room temperature during a loading-unloading cycle with a maximum strain of 1.5% for 0.3~1.8O alloys. The shape of stress-strain curve is highly dependent on the oxygen content. The 0.3O alloy exhibits superelastic recovery with stress hysteresis upon unloading. With increasing oxygen concentration, the apparent yielding stress increased and the stress hysteresis became narrower. Fig. 3-2 shows *in-situ* XRD profiles upon loading and unloading for the 0.3O, 0.6O, 1.2O, 1.5O alloys. The specimen was elongated to the strain of 1.5% and unloaded. XRD measurements were carried out at strains of 0.0%, 0.2%, 0.4%, 0.6%, 0.8%, 1.0%, 1.2%, 1.4% and 1.5%. For the 0.3O alloy, only β phase was detected at a strain of 0.0% (prior to loading). A diffraction peak of the α″ martensitic phase ($202_{\alpha''}$) was detected at a strain of 0.6%, indicating that the apparent yielding of the 0.3O alloy is due to the stress induced martensitic transformation. With increasing applied strain, the intensity of the $202_{\alpha''}$ peak gradually increased while that of the 211_{β} peak decreased. Upon unloading the reverse transformation occurred; the intensity of the 211_{β} peak increased at the expense of the $202_{\alpha''}$ peak. In the alloys with higher oxygen

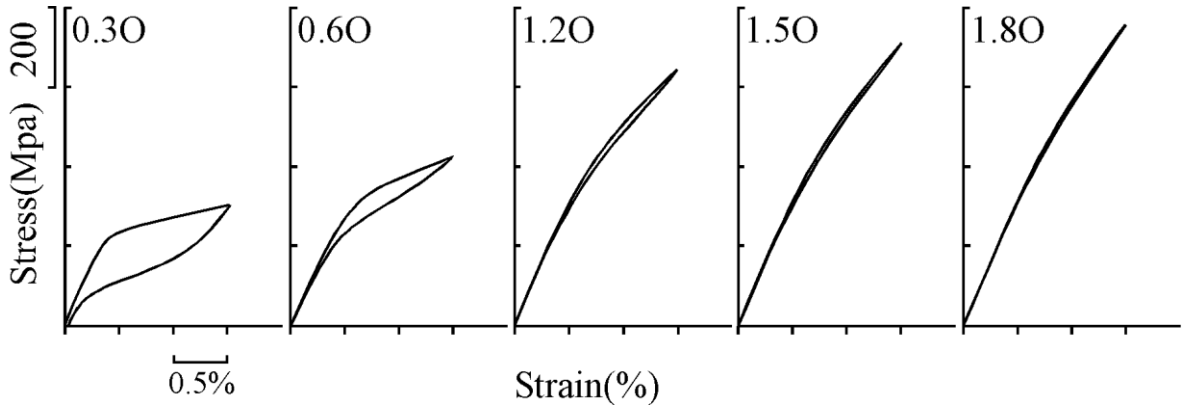

Fig. 3-1. Stress-strain curves obtained at RT for 0.3~1.8O alloys.

concentration, no clear martensitic transformation was detected in all of the loading and unloading process. For example, for the 1.5O alloy, the 211β peak only shifts toward a higher 2θ value at the strain before 0.6% with increasing applied strain. Then with further increasing strain, the 211β peak became broad and shifted toward a higher 2θ value to the strain of 1.5%. Upon unloading this broad peak became sharp again and shifted toward a lower 2θ value until the strain of 0.2% with decreasing applied strain. Finally this sharp peak continued shifting to the original state of prior to loading.

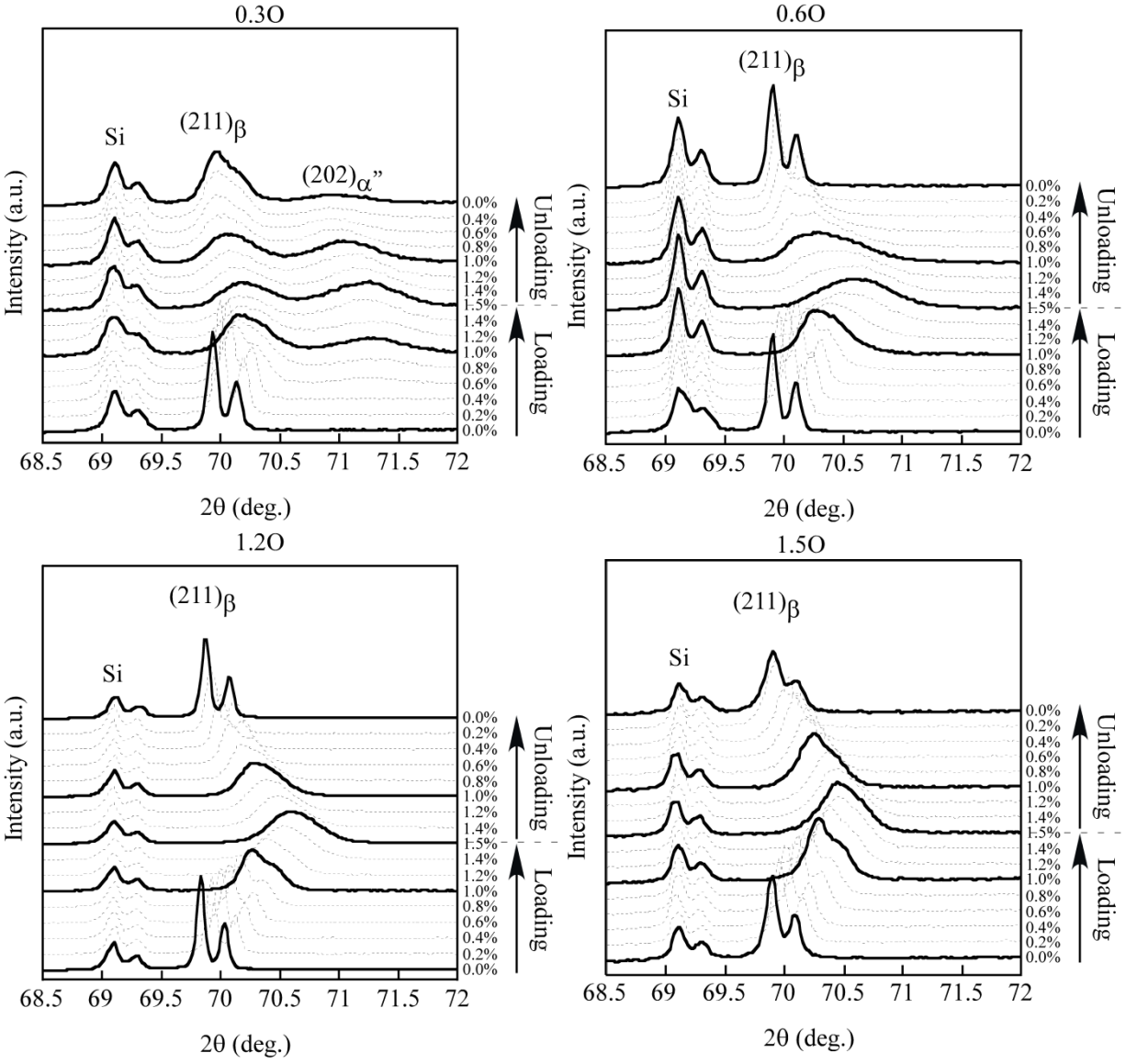

Fig. 3-2. In situ XRD profiles during loading and unloading for 0.3 ~1.5O alloys corresponding to Fig. 3-1.

3.3.2 Deformation behavior

The stress-strain curves for 0.3~1.8O alloys were obtained at temperatures range between 193 and 313K as shown in Fig. 3-3. The tensile stress was applied until the strain reached about 2.5%, and then the stress was removed. The temperature dependence of deformation behaviors are strongly affected by the oxygen concentration. For the 0.3~0.6O alloys, with the deformation temperature increasing to about 233~253K, apparent yielding stress decreased and the stress hysteresis became narrower. Then with further increase in deformation temperature, the yielding stress increased and the stress hysteresis became broader. For the 1.2~1.8O alloys, with increasing deformation temperature the yielding stress increased and the residual strain increased.

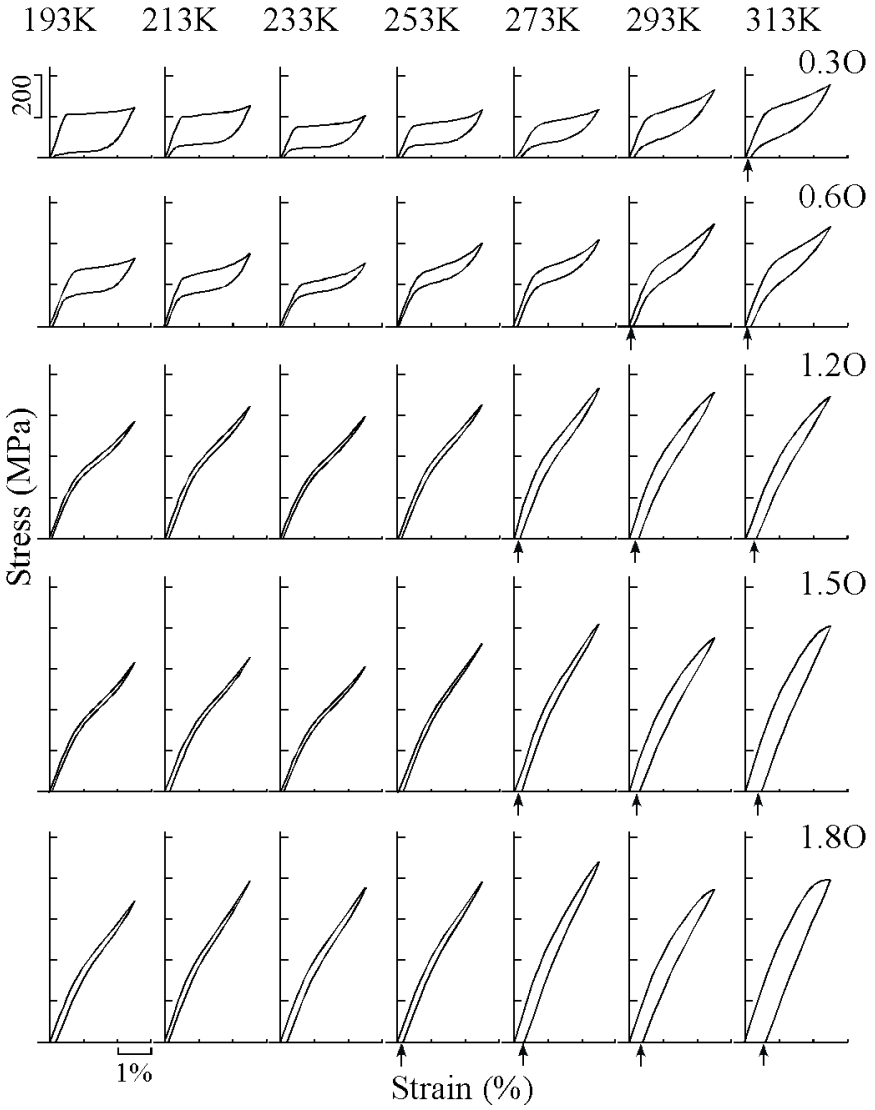

Fig. 3-3. Stress-strain curves obtained at various temperature for 0.3~1.8O alloys.

The yielding stresses derived from tensile tests at various temperatures were plotted as a function of test temperature as shown in Fig. 3-4. The yielding stress increased with increasing oxygen content for each test temperature. It is also noted that the yielding stresses of 0.3~0.6O alloys decreased linearly with increasing test temperature, disobeying Clausius-Clapeyron relationship. Then that of the yielding stresses increased

with slight different slope with further increasing temperature, satisfying Clausius-Clapeyron relationship. For 1.2~1.8O alloys, the yielding stresses only increased linearly with increasing temperature, satisfying the Clausius-Clapeyron relationship.

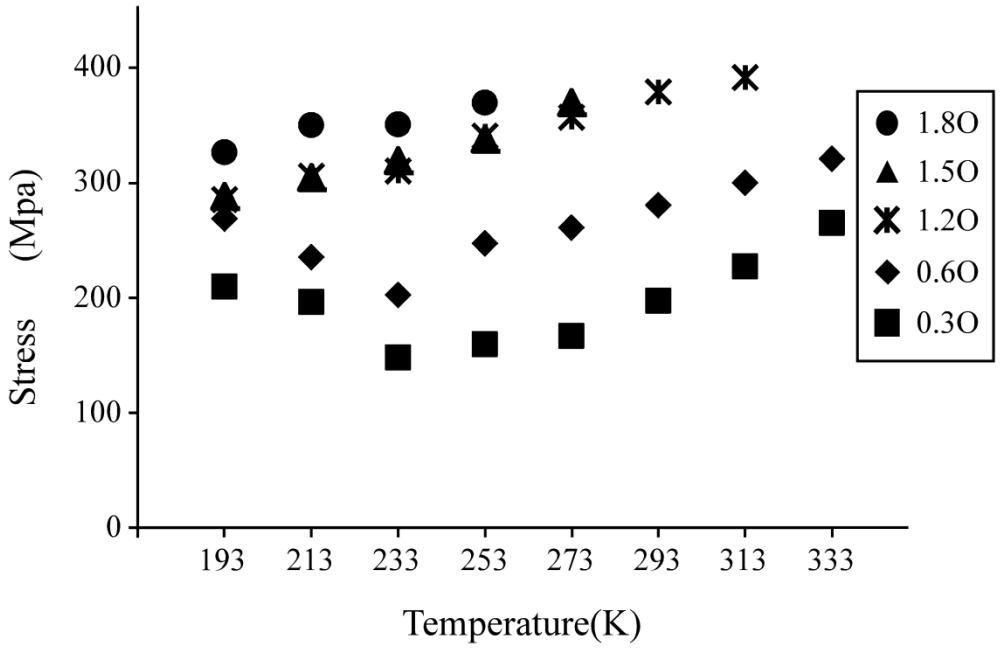

Fig. 3-4. The test temperature dependence on the yielding stresses for 0.3~1.8O alloys.

3.3.3 Microstructure

In order to investigate the microstructure, TEM investigations were carried out for the 0.6, 1.2 and 1.8O alloys and the results are shown in Fig. 3-5. The dark fields and the corresponding selected area diffraction (SAD) patterns of each alloys with the zone axis of $[113]_{\beta}$ are shown together. Diffraction spots corresponding to the ω phase were observed and the intensity of diffuse streaks decreased with increasing oxygen concentration. It is well acknowledged that the ω phase suppresses the martensitic transformation. Dark field images were obtained using the ω phase spots in SAD marked by white circles. The dark field images show that the amount of ω phase decreases with increasing oxygen concentration. The faint contrast is seen in the dark field image of the 1.8O alloy. The electrical resistivity was measured for all the alloys between 200K and 300K with a temperature changing rate of 1 K min^{-1} and the results are shown in Fig. 3-6. For 0.3~1.2O alloys, the relative resistivity increased with decreasing temperature. These anomaly negative tendencies are considered to be associated to the effect of ω phase which suppress the martensitic transformation during cooling [14-21]. With increasing oxygen concentration, the rate of change became weak. These results suggest that lower oxygen concentration alloys are more sensitive with the ω phase during cooling and high oxygen concentration could suppress the formation of the ω phase in the β phase. As a result it is considered that the deviation of the yielding stresses from Clausius-Clapeyron relationship for the 0.3~0.6O alloys shown in Fig. 3-4 is due to the fact that the increase in ω phase raises the yielding stresses during cooling. With increasing oxygen concentration, the effect of ω phase became weaker, resulting in a normal behavior which satisfied the Clausius-Clapeyron relationship due to the suppression from oxygen on ω phase (Fig. 3-6).

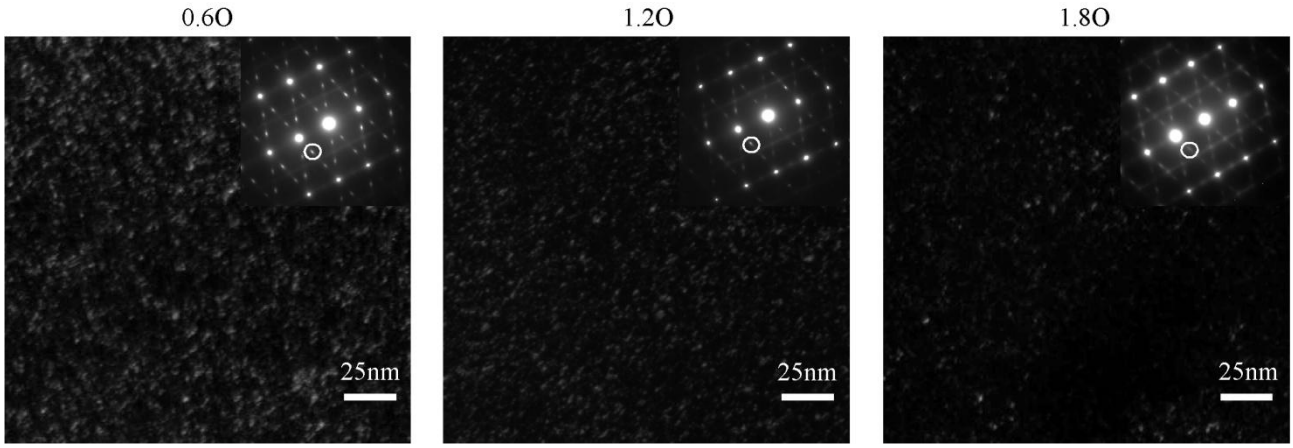

Fig. 3-5. Dark-field image and the corresponding selected area diffraction pattern for 0.6, 1.2 and 1.8O alloys, respectively.

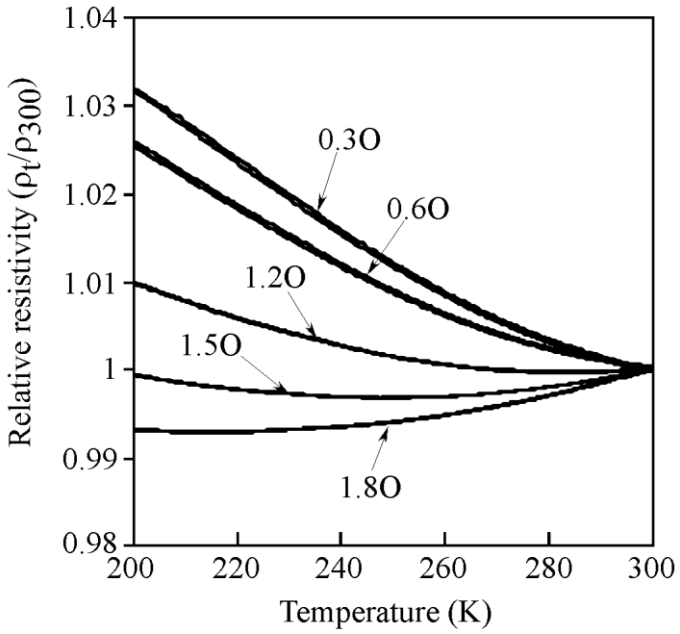

Fig. 3-6. Temperature dependence on relative resistivity (ρ_t/ρ_{300}) in the temperature range between 200 and 300K for 0.3~1.8O alloys.

3.3.4 Mechanism of the deformation behavior

It is proposed that three factors can affect the deformation behavior of the Ti-23Nb-2Zr-0.7Ta-O alloys, i.e. deformation temperature, oxygen concentration and ω phase. In the previous papers [10-13] the nano-domain variants can be induced by interstitial oxygen due to the oxygen occupy octahedral lattice to leading to $\{1\,\bar{1}0\}$ plane shuffled along the <110> direction. These nano-domain variants distribute equivalently in the annealed alloys because there is no external stress. The increase in oxygen concentration raises the amount of nano-domain. It is supposed that for the 0.3O alloy, the lattice distortion strain became larger with increasing applied strain. When the applied stress becomes strong enough to break the balance of the stress field the interstitial oxygen moves into other site of lattice in order to release the elastic energy. The growth of a favorable variant of nano-domain along the tensile direction overcomes the local stress field from other nano-domain variants. As a result a large martensitic transformation occurs (Fig. 3-2). Reverse martensitic transformation occurs during unloading. The self-accommodate of the variants occurs but small amount of residual martensite phase was still remained at a strain of 0.0% (after unloading). For the 0.6O alloy in Fig. 3-7, only the growth of lattice distortion strain occurred and martensite phase is difficult to form due to the increase of the amount of nano-domain. The local stress field becomes stronger to be difficult to overcome. Only the growth of the favorable nano-domain variant becomes large. With further increasing oxygen concentration (Fig. 3-7 for high oxygen concentration alloys), i.e. 1.2~1.8O alloy, no phase transformation occurs and only the lattice distortion strain increases with increasing applied strain similar to the 0.6O alloy. The lattice distortion strain is expected to be smaller than that of the 0.6O alloy. It is because the local stress field becomes stronger due to the increase in the amount of nano-domains. It is hence considered that the broad peak shown in Fig. 3-2 is associated with the nano-domain structure. Similar

behavior was also reported in the binary Ti-Nb alloy with interstitial oxygen atoms [12, 13]. The ω phase also affects the deformation behavior of alloys. Fig. 3-5 shows that the increase in the oxygen concentration decreases the amount of ω phase. The amount of ω phase is also affected by the temperature. Tane et al. [8] showed that the martensite phase and ω phase increased upon cooling. It was also reported that the ω transformation is reversible upon heating and cooling [14]. It is considered that the increase in the apparent yielding stress with decreasing test temperature in lower oxygen concentration alloys is due to the formation of athermal ω phase. With increasing the oxygen concentration, the yielding stresses decreased linearly satisfying the Clausius-Clapeyron relationship due to the suppression of the ω phase during cooling.

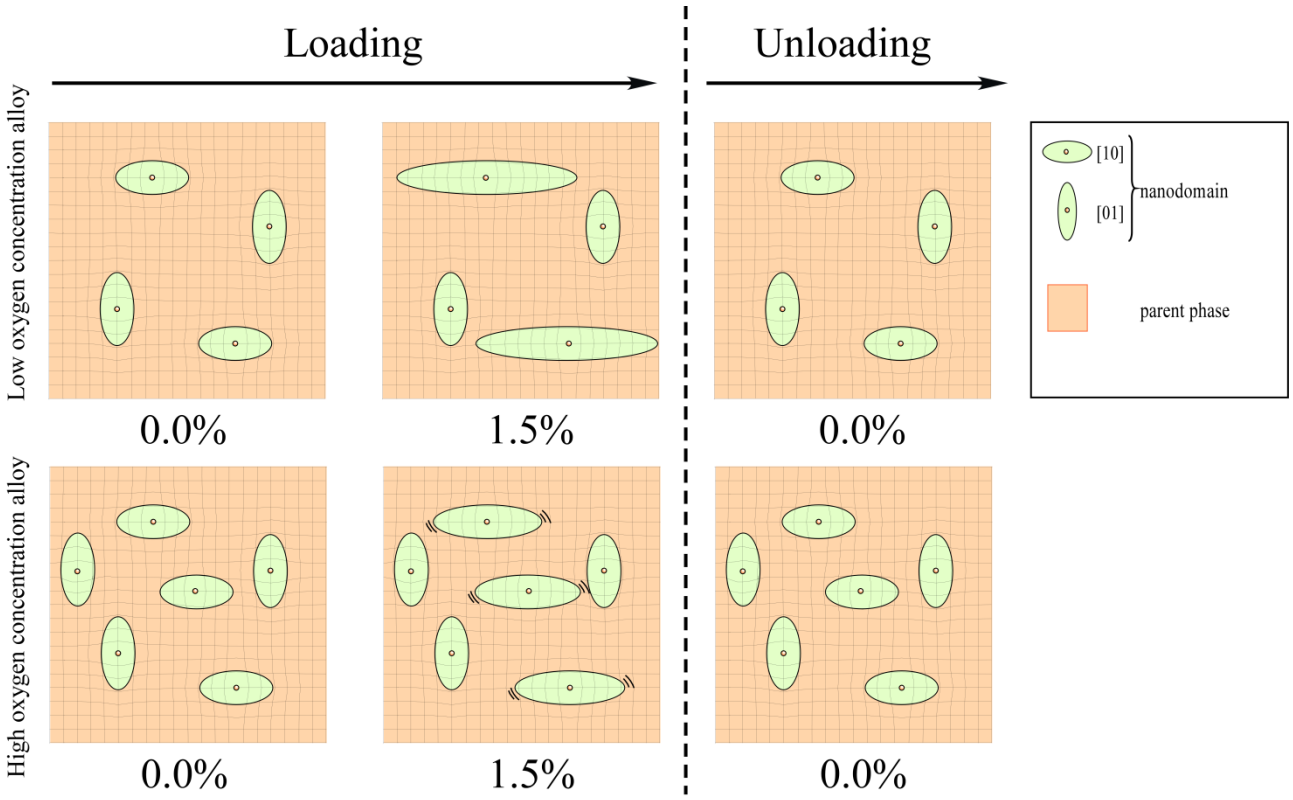

Fig. 3-7. The schematic illustration for the change of two nano-domain variants with loading and unloading for 0.6~1.8O alloys.

3.4 Conclusion

In summary, the deformation behaviors of a group of Ti-23Nb-2Zr-0.7Ta-*x*O (at %) (*x*=0.3, 0.6, 1.2, 1.5, 1.8) alloys were investigated centered on the effects of temperatures, the oxygen concentration and the ω phase by Tensile test, TEM and *in situ* XRD. The results are summarized as follows.

1. The shape of stress-strain curve was highly dependent on the oxygen concentration. The 0.3O alloy exhibited superelastic recovery with stress hysteresis upon unloading. With increasing oxygen concentration in 0.6~1.8O alloys, the apparent yielding stress increased and the stress hysteresis became narrower.
2. The apparent yielding stress decreased linearly with decreasing test temperature in 1.2~1.8O alloys satisfying Clausius-Clapeyron relationship. In the 0.3~0.6O alloys, the apparent yielding stress decreased with decreasing test temperature at higher temperatures, but the yielding stress increased with decreasing test temperature at lower temperature region.
3. For 0.3~1.2O alloys, the relative resistivity increased with decreasing temperature where the rate of change became weak with increasing oxygen concentration, implying that the oxygen suppresses the formation of athermal ω phase. It is suggested that the increase in the apparent yielding stress with decreasing test temperature in lower oxygen concentration alloys is due to the formation of athermal ω phase.
4. The deformation mechanism of the alloys is strongly dependent on oxygen concentration. For the low oxygen content of 0.3 O alloys, the lattice distortion strain became larger with increasing applied strain and finally come into being martensite phase because the growth of a favorable variant of nano-domain

along the tensile direction overcomes the local stress field from other variants of nano-domain to release the external stress. With increasing oxygen concentration for 0.6~1.8O alloys, no phase transformation occurred and only the lattice distortion strain increased by the growth of favorable nano-domain variant with increasing applied strain because the local stress field by oxygen is too strong to be overcome.

References

[1] T. Saito, T. Furuta, J.H. Hwang, S. Kuramoto, K. Nishino, N. Suzuki, R. Chen, A. Yamada, K. Ito, Y. Seno, T. Nonaka, H. Ikehata, N. Nagasako, C. Iwamoto, Y. Ikuhara, T. Sakuma, Sci. 300 (2003) 464-467.

[2] M.Y. Gutkin, T. Ishizaki, S. Kuramoto, I.A. Ovid'ko, Acta Mater. 54 (2006) 2489-2499.

[3] H. Xing, J. Sun, Q. Yao, W.Y. Guo, R. Chen, Appl. Phys. Lett. 92 (2008) 151905.

[4] R.J. Talling, R.J. Dashwood, M. Jackson, D. Dye, Acta Mater. 57 (2009) 1188-1198.

[5] M. Besse, P. Castany, T. Gloriant, Acta Mater. 59 (2011), p. 5982

[6] Y. Yang, G.P. Li, G.M. Cheng, Y.L. Li, K. Yang, Appl. Phys. Lett. 94 (2009), p. 061901.

[7] T. Yano, Y. Murakami, D. Shindo, S. Kuramoto, Acta Mater. 57 (2009), p. 628

[8] M. Tane, T. Nakano, S. Kuramoto, M. Hara, M. Niinomi, N. Takesue, T. Yano, H. Nakajima, Acta Mater. 59 (2011), p. 6975

[9] E.G. Obbard, Y.L. Hao, R.J. Talling, S.J. Li, Y.W. Zhang, D. Dye, R. Yang, Acta Mater. 59 (2011), p. 112

[10] H.Y. Kim, L.S. Wei, S. Kobayashi, M. Tahara, S. Miyazaki, Acta Mater. 61 (2013), p. 4874

[11] L.S. Wei, H.Y. Kim, S. Miyazaki, Acta Mater. 100 (2015), p. 313

[12] Y. Nii, T. Arima, H.Y. Kim, S. Miyazaki, Phys. Rev. B. 82 (2010), p. 214104

[13] M. Tahara, H.Y. Kim, T. Inamura, H. Hosoda, S. Miyazaki, Acta Mater. 59 (2011), p. 6208

[14] Y. Al-Zain, H.Y. Kim, T. Koyano, H. Hosoda, T.H. Nam, S. Miyazaki, Acta Mater, 59 (2011), p. 1464

[15] Y. Al-Zain, H.Y. Kim, T. Koyano, H. Hosoda, S. Miyazaki, Scripta Mater, 103 (2015), p. 37

[16] D.J. Cometto, G.L. Houze, R.F. Hehemann, Trans Metall Soc AIME, 233 (1965), p. 30

[17] J.C. Ho, E.W. Collings, Phys Rev B, 6 (1972), p. 3727

[18] C. Hayman, W.W. Gerberich, Metall Trans A, 16A (1985), p. 187

[19] Y. Hariharan, M.P. Janawadker, T.S. Radhakrishnan, Solid State Commun, 59 (1986), p. 127

[20] D. Stewart, B.A. Hatt, J.A. Roberts, Brit J Appl Phys, 16 (1965), p. 1081

[21] A.J. Perkins, P.E. Yaffe, R.F. Hehemann, Metal Trans, 1 (1970), p. 2785

Acknowledgements

How time flies fast! Six years have passed for me since I joined in this laboratory. These six years will be my important experience stage in my school days. I learned not only essential knowledge, research skills, but also how to rely on willpower and finally to make my dream come true. These became possible as Prof. Kim and Prof. Miyazaki have usually encouraged me. It is not the end but merely a beginning. I hope and pray I will work hard with more success in the future and never give up.

It gives me great pleasure to acknowledge Prof. Kim for his kind help and useful advices on my research. Prof. Kim's ability and intelligence surpass the average and affected me deeply. I am pleasure to express my deep sense of thanks and gratitude to Prof. Kim, because he always encouraged me and gave me the hope to make me bolstered confidence when I lose my heart on the research. Actually I am glad to talk with Prof. Kim about everything with which I could learn a lot from his professional way to think. I am grateful to Prof. Kim for the so many times he spent to revise my papers. I will never forget Prof. Kim's kind enlightenment and help.

It is a genuine pleasure to express my deep sense of thanks and gratitude to Prof. Miyazaki for the invaluable suggestions and useful discussions when I lost my mind and for the cordial encouragement when I failed. Even a little praise and encouragement from him, the impact on me is sometimes lifelong. Prof. Miyazaki unreservedly passed on to me his knowledge and set good examples and cultivated virtues to me how to be a devoted and conscientious researcher. This will benefit me throughout the research year. Prof. Miyazaki also impacted on me how to deal with and overcome the difficulties and made me turn my dream of a lifetime into reality. I am very grateful to Prof. Miyazaki to recommend me to garner the Japanese Government Scholarship to pursue my higher studies. I think I am a lucky girl to be a student of Prof.

Miyazaki.

I am really thankful to Prof Tanimoto, Prof Koyano and Prof Mitarai for their comments and valuable suggestions during my defense which really helped me to refine my PhD thesis.

I am really thankful to my dear parents, sister and husband for their supports and encouragement. I will never forget my husband to cook for me delicious foods every day and help me doing my experiments all time. I am also thankful to my parents and sister always standing by me with their thick-and-thin hearts.

I am thankful to Mr Fu for helping me in preparation for the entrance examination. Many thanks for his kind comments and support. I always can gain some good deal of enlightenment from him. Thanks so much for being such a close friend and colleague.

I am thankful to the present students in this laboratory for all the support and concern: Mr Nakamura, Mr Watahiki and Mr Kaitsuka, thank you for all the help and cooperation. Good luck for their new stage as a social man in new company. Mr Okabe, Mr Komamura, Mr Terada, Mr Hattori and Mr Furukawa, many thanks for their support and help and wish them get more excellent results in your research and find a good job. Mr Amemiya, Mr Iida and Mr Suzuki, wish them all the luck in their studies and get excellent results.

I thank profusely Institute of Materials Science, University of Tsukuba for providing a favorable research condition.

February, 2016

WEILESI

List of publications

1. L.S. Wei, H.Y. Kim, S. Miyazaki. Effects of oxygen concentration and phase stability on nano-domain structure and thermal expansion behavior of Ti–Nb–Zr–Ta–O alloys, Acta Materialia. 100 (2015), 313-322.

2. H.Y. Kim, L.S. Wei, S. Kobayashi, M. Tahara, S. Miyazaki. Nano-domain structure and its effect on abnormal thermal expansion behavior of a Ti-23Nb-2Zr-0.7Ta-1.2O alloy, Acta Materialia, 61 (2013), 4874-4886.

3. L.S. Wei, H.Y. Kim, S. Miyazaki. Effect of oxygen concentration and thermal expansion behavior of Gum Metal, 2013 The Japan Institute of Metals and Materials Spring Annual Meeting, p.232

4. L.S. Wei, H.Y. Kim, S. Miyazaki. Nano-domain structure and effects of oxygen and Nb concentration on Ti-Nb-Zr-Ta-O alloy, 2015 The Japan Institute of Metals and Materials Spring Annual Meeting, J.16